minerals

MDPI

Article

Petrogenesis and Tectonic Implications of Early Paleozoic Magmatism in Awen Gold District, South Section of the Truong Son Orogenic Belt, Laos

Zhi Shang and Yongqing Chen *

School of Earth Sciences and Resources, China University of Geosciences, Beijing 100083, China; shangzhi6609@163.com

* Correspondence: yqchen@cugb.edu.cn

Abstract: The Truong Son orogenic belt (TSOB) is one of the most important orogenic belts in the Indochina block. There are numerous mafic to felsic intrusions in the Early Paleozoic caused by the Tethyan orogeny. However, the tectono-magmatic evolution of the TSOB in the Early Paleozoic is still unclear. In this paper, zircon U-Pb dating, whole-rock geochemistry, and the Sr-Nd isotopic data of the Early Paleozoic magmatic rocks have been systematically investigated to explore the petrogenesis and tectonic significance of these rocks in the TSOB. Based on our new results integrated with previous geological data, four major tectono-magmatic episodes are identified. (1) The Middle Cambrian (~507 Ma) is the early stage of northward subduction of the Tamky-Phuoc Son Ocean. (2) The Early Ordovician to Middle Ordovician (483–461 Ma) is the main subduction stage of the Tamky-Phuoc Son Ocean. The intrusive rock associations imply the closure of the Tamky-Phuoc Son Ocean. (3) The Late Ordovician to Early Silurian (461–438 Ma) is the collision stage of the Kontum massif and Truong Son terrane. (4) The Early Silurian to Late Silurian (438–410 Ma) is the late stage of collision accompanied by slab roll-back.

Keywords: Truong Son orogenic belt; zircon U-Pb age; Sr-Nd isotopes; tectonic significance; Early Paleozoic; Laos

Citation: Shang, Z.; Chen, Y. Petrogenesis and Tectonic Implications of Early Paleozoic Magmatism in Awen Gold District, South Section of the Truong Son Orogenic Belt, Laos. *Minerals* **2022**, *12*, 923. https://doi.org/10.3390/min12080923

Academic Editor: Tatsuki Tsujimori

Received: 26 June 2022
Accepted: 20 July 2022
Published: 22 July 2022

1. Introduction

The Truong Son orogenic belt (TSOB) intersecting central Vietnam and northeastern Laos is one of the most important tectonic and metallogenic belts in the Indochina block. Numerous mafic to felsic magmatic intrusions can be found in this zone. These intrusions are closely related to the tectonic evolution of the Tamky-Phuoc Son Ocean and the Song Ma Ocean [1–4]. The Early Paleozoic magmatism is mainly distributed in the southern TSOB.

The south margin of the TSOB is the Tamky-Phuoc Son suture zone (TPSSZ), which is separate from the Kontum Massif. It is commonly suggested that the extensive magmatism in the southern TSOB is mainly of the Early Paleozoic and the Early Mesozoic [5–12]. The viewpoints toward the tectonic evolution and the formation of magmatism in the Early Mesozoic have reached a consensus [13], whereas the cause of the generation of the magmatism in the Early Paleozoic is still unclear. In particular, the nature and timing of different tectonic stages remain indistinct. Many researchers have focused on the Kontum massif, which is located in the south of the TPSSZ, whereas little attention has been paid to the southern TSOB because of the extremely low degree of geological work. The weak research of the southern TSOB directly resulted in the genetic links being unclear between the Tethyan orogeny and tectono-magmatic evolution of the southern TSOB in the Early Paleozoic.

This article focuses on the Awen gold deposit, a newly discovered deposit in recent years in the southern TSOB in Laos and the surrounding areas. Different kinds of magmatic rocks were systematically collected in the southern TSOB, including 9 samples for zircon U-Pb dating, 56 samples for major and trace element analyses, and 9 samples for whole-rock Sr and Nd isotope analyses. We integrate these new data with published data to discuss the petrogenesis, magma source, and tectonic significance of these magmatic rocks in the southern TSOB. Our new research provides a summary of the tectonic evolutionary history of the southern TSOB in the Tethyan orogeny and further constrains these events in this region.

2. Geological Setting

The Indochina block is one of the largest continental blocks in Southeast Asia, occupying a large part of the Indochina peninsula. During the Early Paleozoic, the Indochina block and other Southeast Asia blocks were adjacent to the Gondwanaland [14–16]. The eastern margin of the Indochina block is composed of the NW-trending TSOB and the Kontum massif. The TSOB is bounded by the Song Ma suture zone to the northeast separated from the South China block and the TPSSZ to the south separated from the Kontum Massif, and the Dien Bien Phu suture zone to the northwest separated from the Simao-Changdu block (Figure 1). Previous studies have investigated the evolution of the TSOB in southern Laos and the adjacent Kontum massif. Nagy et al. [12] and Hutchison [17] proposed that the magmatism in the Early Paleozoic was formed by the split and northward subduction of the Indochina block from Gondwanaland in Ordovician-Silurian, while Carter et al. [11] argued the Early Paleozoic magmatism was related to the extensional tectonic setting before the breakup of Gondwanaland. Nakano et al. [18] hold the viewpoint that the Early Paleozoic magmatism was formed in an active continental margin before the collision between South China and the Indochina blocks. Faure et al. [13] considered the Early Paleozoic magmatism to be the product of the intracontinental orogeny of the South China block.

The TSOB is a complex, faulted region. The strata in this area are mainly composed of Ordovician to Cretaceous sedimentary and subvolcanic rocks, and the strata after the Jurassic are sporadically outcropped [4,19]. The Ordovician-Devonian formation is primarily composed of epimetamorphic mudstone and sandstone. These units are unconformably overlain by Carboniferous-Permian carbonate formations. Since the Triassic, the strata have mainly been comprised of terrestrial red bed sedimentation. The strata of the Middle Ordovician-Devonian are strongly folded [4]. The deep faults in this belt are NW-trending, and some of them show dextral strike-slip kinematics [20]. The magmatic rocks in this belt trend NW and were formed in Paleozoic and Mesozoic [3,4]. Cenozoic volcanic rocks are outcropped in the south of the belt [7]. The complex tectono-magmatic evolutionary history makes this area an important metallogenic belt, namely, the TSOB.

The Awen gold deposit is a newly discovered gold deposit in recent years in the southern TSOB that has large metallogenic prospects (Figures 1 and 2). It is located at the intersection of the TPSSZ and the Po Ko suture zone where abundant structures and magmatic rocks developed. The metallogenic condition is good. The sedimentary formation in this district is mainly a group of epimetamorphic turbidite incorporating sandy slate, silt slate, metasandstone, and phyllite. The complicated structure system in this area is mainly composed of thrust faults. These faults can be generally subdivided into NW and nearly E-W trending groups (Figure 2).

Figure 1. Map of Southeast Asia showing the extent of the Indochina Block. DBF—Dien Bien Phu Fault; RRF—Red River Fault; SCF—Song Ca Fault; TPF—Three Pagodas Fault; and WCF—Wang Chao Fault. Modified after [5].

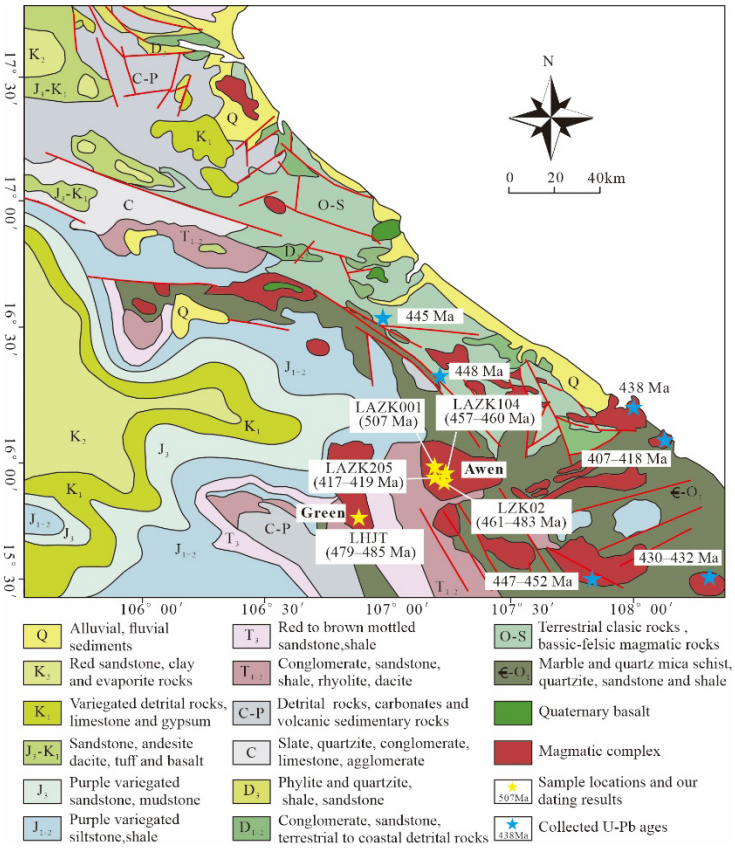

Figure 2. Geologic sketch map and sample locations. Reprinted with permission from Ref. [2]. 2022, Ce Wang. U-Pb ages are from [2,6,8,11,21] and this study.

3. Materials and Methods

3.1. Sample Petrography

The magmatism in the southern TSOB was extensive. These magmatic rocks comprise basalt, gabbro, diorite, and quartz monzonite. In this study, we systematically investigated the magmatic rocks of the Awen magmatic complex and green pluton. The olivine-basalt, quartz-monzonite, granodiorite, and tonalite samples were collected from the Awen magmatic complex. The gabbro was sampled from green pluton. Their petrologic characteristics are given below.

3.1.1. Gabbro/Olivine-Basalt

The gabbro (LHJT) is gray-green and has gabbroic texture. The major minerals are plagioclase (43%), pyroxene (9%), and a small amount of amphibole and biotite (3%). Auxiliary minerals are mainly magnetite and Fe-Ti oxide minerals. These rocks are weakly altered. The olivine-basalt (LAZK001) is dark green and has a porphyritic texture. Phenocryst is primarily composed of olivine (18%) and plagioclase (17%). The olivine is granular (Figure 3a). The major minerals of the matrix are mainly composed of pyroxene, plagioclase, and minor olivine. Accessory minerals include zircon and magnetite.

3.1.2. Quartz-Monzonite

The quartz-monzonite (LZK02) is mainly composed of plagioclase (32%), K-feldspar (36%), and quartz (9%). The plagioclase is euhedral tabular and exhibits a clear polysynthetic twin (Figure 3b). The K-feldspar is characterized by a Carlsbad twin. Quartz is granular and mainly distributed in the gaps of feldspar.

3.1.3. Granodiorite

The granodiorite (LAZK104) is dark gray and has a porphyaceous texture. The major minerals are plagioclase (47%), K-feldspar (10%), quartz (18%), and biotite (5%). The plagioclase display subhedral boards and polysynthetic twins with a degree of sericitization. Micro-granular quartz and feldspar are the principle components of the groundmass. Accessory minerals are zircon, magnetite, and titanite (Figure 3c).

3.1.4. Tonalite

The tonalite (LAZK205) is light green to gray and has a porphyritic texture with euhedral to subhedral plagioclase and K-feldspar phenocryst (Figure 3d). Major minerals mainly consist of plagioclase (55%), K-feldspar (10%), quartz (20%), and biotite (5%). Plagioclase exhibits an obvious polysynthetic twin. The Carlsbad twin is obvious in the K-feldspar. The size of the quartz varies from fine to coarse. Accessory minerals comprise titanite, apatite, and zircon.

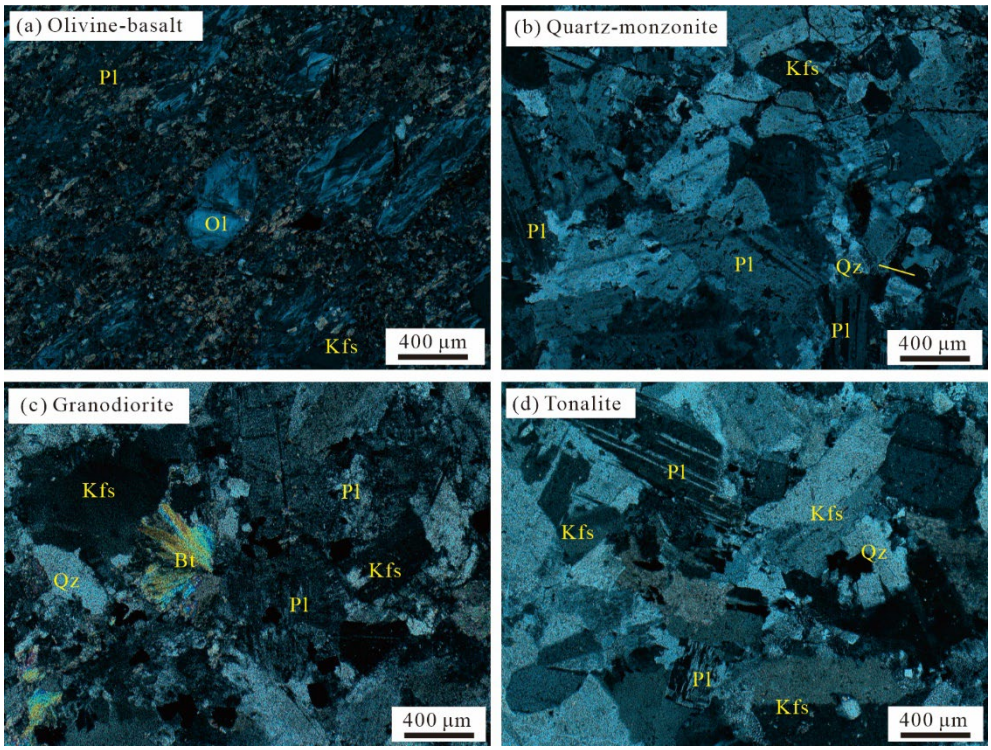

Figure 3. Representative photomicrographs (cross-polarized light) of thin sections of the olivine-basalt (**a**), quartz-monzonite (**b**), granodiorite (**c**), and tonalite (**d**). Kfs—K-feldspar; Pl—plagioclase; Qz—quartz; and Ol—olivine.

3.2. Zircon Dating

Zircon U-Pb analyses were accomplished at the Continental Tectonics and Dynamics Laboratory of Institute of Geology, Chinese Academy of Geological Sciences. U-Pb abundance was measured by the latest Neptune Plus multiple collector (ICP-MS) of Thermo Fisher Co., Ltd. (Waltham, MA, USA). The laser-ablation system used in the measurement was developed by the GeoLasPro 193 nm invented by the U.S. Coherent Co., Ltd. (Santa Clara, CA, USA). Helium was used as a carrier gas to enhance the transport efficiency of the ablated material. The spot size of the laser ablation beam in this study was 32 μm. The LA-ICP-MS operating conditions were optimized with the measurements of reference zircon 91500. The accuracy of the data was verified by using GJ-1 as an auxiliary standard. The LA-ICP-MS measurement was carried out using a time-resolved analysis operated in fast peak-hopping and the DUAL detector mode using a short integration time. The Harvard standard zircon 91500 and GJ-1 were measured for every 5–10 sample spots. The obtained weighted average $^{206}Pb/^{238}U$ ages in 15 analyses of GJ-1 and 17 analyses of 91500 are 603.2 ± 3.8 Ma and 1063.5 ± 1.8 Ma, respectively, in this study, which are consistent with the reference age of 599.8 ± 1.7 Ma and 1062.4 ± 0.8 Ma [22,23]. The data were calculated by the ICPMSDataCal program [24] and the Isoplot program [25].

3.3. Major and Trace Elements

Whole-rock major and trace element analyses were measured at the Testing Center of Rocks and Minerals in Henan. The major elements were analyzed using a ZSX100e (Rigaku Co., Akishima, Tokyo, Japan) X-ray fluorescence spectrometer (XRF) on fused glass beads. The trace elements, including rare earth elements, were measured by inductively coupled plasma mass spectrometry (ICP-MS) with an XSERIES2 (Thermo Fisher Co., Ltd., Waltham, MA, USA). The detection limits meet the national standard DD2005-01. The analysis results of international standards were in agreement with the recommended values, indicating that the precision and accuracy were better than 1.5% for all elements.

3.4. Whole Rock Sr and Nd Isotopes

The Sr-Nd isotope analyses were carried out at the MOE Key Laboratory of Orogenic Belts and Crustal Evolution, Peking University. Powdered bulk-rock samples were first spiked with mixed isotope tracers and then dissolved in a solution of hydrofluoric and nitric acid in Teflon capsules before Rb-Sr and Sm-Nd isotope analyses. Rb, Sr, Sm, and Nd were separated using conventional ion exchange procedures, as described by Yan et al. [26]. The Sr-Nd isotopes were measured on a VG Axiom mass spectrometer. The Nd and Sr ratios were normalized to $^{146}Nd/^{144}Nd = 0.7219$ and $^{86}Sr/^{88}Sr = 0.1194$, respectively. The BCR-2 standards with $^{143}Nd/^{144}Nd = 0.512633 \pm 0.000017$ (2σ) and $^{87}Sr/^{86}Sr = 0.705013 \pm 0.000019$ (2σ), respectively, were used to assess analytical precision. The initial $^{87}Sr/^{86}Sr$ and $^{143}Nd/^{144}Nd$ ratios were calculated using their zircon U-Pb ages.

4. Results

4.1. Zircon U-Pb Ages

Nine representative samples collected from the southern TSOB were analyzed for zircon U-Pb dating in this study. The zircon U-Pb data are shown in Supplementary Table S1. The majority of the zircon grains are light gray, euhedral, and transparent under the microscope. These grains are 70–120 μm in length, with elongation ratios ranging from 1.2:1 to 4.0:1. Almost all of these zircons exhibit oscillatory growth zoning (Figure 4), implying their magmatic origin.

4.1.1. Awen Magmatic Complex

Olivine-basalt: The Th and U concentrations of zircons for sample LAZK001-01 are 42–4725 ppm and 188–2798 ppm, respectively, with the Th/U ratios of 0.07–4.30. Twenty-nine spots are tested with thirteen analyzed spots discarded due to low concordance, yielding a weighted mean $^{206}Pb/^{238}U$ age of 507.0 ± 13.0 Ma (MSWD = 2.0) (Figure 4a).

Quartz-monzonite: The contents of Th and U in zircons of sample LZK02-01 are 184–901 ppm and 322–1013 ppm with the Th/U ratios of 0.57–0.96. Thirty-two spots from sample LZK02-01 are analyzed with three spots discarded, producing a weighted mean $^{206}Pb/^{238}U$ age of 461.4 ± 2.2 Ma (MSWD = 1.3) (Figure 4d). The distribution of the concentrations of Th and U in the zircons of sample LZK02-02 are 61–1166 ppm and 456–1428 ppm. The Th/U ratios range from 0.06 to 1.08. Thirty zircon spots from sample LZK02-02 are tested with eight discordant spots discarded, providing a weighted mean $^{206}Pb/^{238}U$ age of 483.3 ± 2.6 Ma (MSWD = 1.4) (Figure 4e).

Granodiorite: The zircons in sample LAZK104-1 have Th and U contents of 446–1111 ppm and 647–1215 ppm, with Th/U ratios of 0.63–0.98. Thirty zircons from sample LAZK104-1 are tested, providing a weighted mean $^{206}Pb/^{238}U$ age of 459.9 ± 1.4 Ma (MSWD = 0.46) (Figure 4f). The distribution of the concentrations of Th and U in zircons of sample LAZK104-2 are 411–3016 ppm and 515–2810 ppm, and the Th/U ratios range from 0.67 to 1.16. The weighted mean $^{206}Pb/^{238}U$ age of sample LAZK104-2 is 456.9 ± 1.2 Ma (MSWD = 0.7) (Figure 4g) in 35 spots, with one discordant spot discarded.

Tonalite: The Th and U concentrations of zircons from sample LAZK205-01 are 799–7099 ppm and 913–4594 ppm, respectively, with the Th/U ratios of 0.85–1.81. The zircons in sample LAZK205-02 have Th and U contents of 564–4988 ppm and 643–3136 ppm, respectively, with the Th/U ratios of 0.88–1.66. Forty spots for sample LAZK205-01 with two spots discarded yield a weighted mean $^{206}Pb/^{238}U$ age of 417.1 ± 6.2 Ma (MSWD = 3.0) (Figure 4h). Forty spots were analyzed, with one spot discarded, yielding a weighted mean $^{206}Pb/^{238}U$ age of 419.0 ± 7.0 Ma (MSWD = 2.2) (Figure 4i) for sample LAZK205-02.

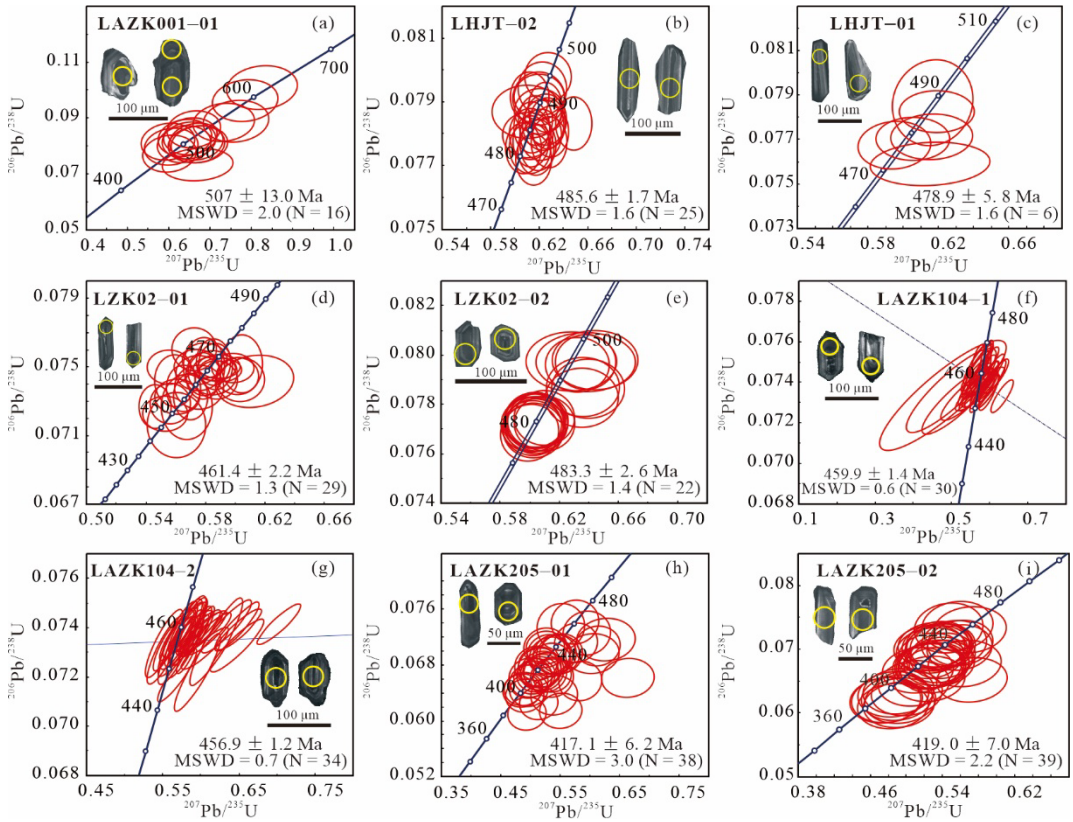

Figure 4. LA-ICP-MS zircon U-Pb concordia diagrams and cathodoluminescence (CL) images of representative zircons for the dated samples from the southern TSOB. Sample locations are shown in Figure 2. (**a**) olivine-basalt; (**b**,**c**) gabbro; (**d**,**e**) quartz-monzonite; (**f**,**g**) granodiorite; (**h**,**i**) tonalite.

4.1.2. Green Pluton

Gabbro: The measured zircons of sample LHJT-01 have Th and U contents of 77–1324 ppm and 301–4454 ppm, respectively. The Th/U ratios are between 0.07 and 0.75. Fifteen spots are measured with nine spots discarded due to low concordance, providing a weighted mean $^{206}Pb/^{238}U$ age of 478.9 ± 5.8 Ma (MSWD = 1.6) (Figure 4c). The Th and U concentrations of zircons from sample LHJT-02 are 33–446 ppm and 200–881 ppm, respectively, with the Th/U ratios of 0.06–0.57. Thirty-one spots for sample LHJT-02 yield a weighted mean $^{206}Pb/^{238}U$ age of 485.6 ± 1.7 Ma (MSWD = 1.6) (Figure 4b), with six spots discarded due to low concordance.

4.2. Major and Trace Elements

Fifty-six fresh samples were measured for whole-rock major and trace element analyses (data are shown in Supplementary Table S2). These samples were collected from the Awen magmatic complex and green pluton, respectively.

4.2.1. Awen Magmatic Complex

Olivine-basalt: These samples are plotted in the gabbro field (Figure 5a) and belong to the potassic basalt series in Figure 5b. The major element contents are SiO_2 = 36.81%–42.03%, Al_2O_3 = 8.03%–9.16%, MgO = 21.03%–23.14%, and TFe_2O_3 = 17.36%–19.90%. The Mg# values (molar Mg/[Mg + Fe]) range from 0.72 to 0.74. For the rare earth element (REE), ∑REE = 70.38–102.03 ppm. The La_N/Yb_N values vary from 4.72 to 7.87. All these samples show moderate to negligible negative Eu anomalies ([w(Eu)/w(Eu*)]). In the chondrite-normalized REE diagram (Figure 6), light rare earth element (LREE) exhibits slight enrichment. These olivine-basalt samples are characterized by being enriched in Th, U, and Pb

and depleted in Rb, Ba, Nb, Ta, and Ti, as shown in the primitive mantle normalized trace element diagram (Figure 6).

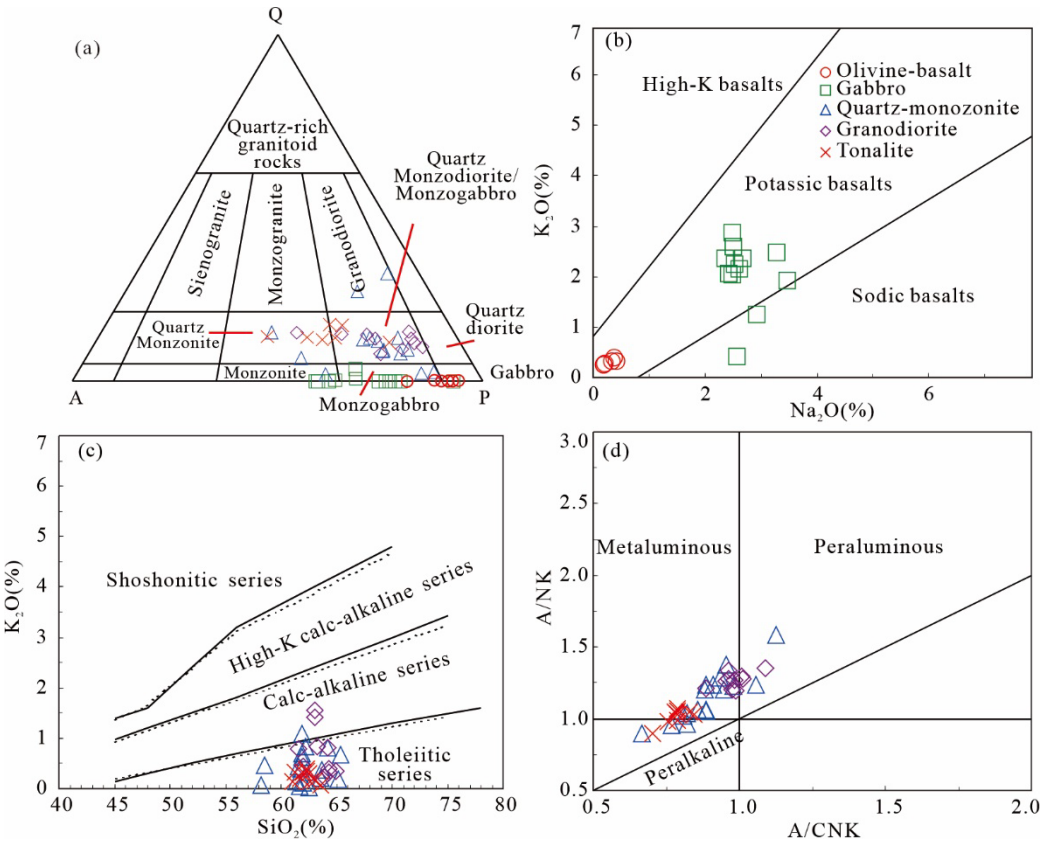

Figure 5. (**a**) QAP diagram after [27]; (**b**) Na_2O vs. K_2O diagram after [28]; (**c**) SiO_2 vs. K_2O diagram after [29]; and (**d**) molar Al/(Ca + Na + K) vs. Al/(Na + K) diagram after [30].

Granodiorite and quartz-monzonite: These samples are plotted in the field of quartz-monzodiorite on the QAP diagram (Figure 5a). The majority of the samples are tholeiitic series (Figure 5c). The A/CNK values range from 0.67 to 1.35, presenting metaluminous signatures (Figure 5d). The contents of SiO_2 range from 58.22 to 65.35%, of Al_2O_3 range from 15.27 to 17.24%, of MgO range from 1.08 to 2.98%, and of TFe_2O_3 range from 3.98 to 17.15%. The LREE is relatively enriched with moderate negative Eu anomalies (δEu = 0.65–1.06). ∑REE = 54.89–186.14 ppm, La_N/Yb_N = 2.67–18.57. The characteristics of trace elements are enriched in Th, U, Pb, Zr, and Hf and depleted in Rb, Ba, Sr, Nb, Ta, and Ti (Figure 6).

Tonalite: These samples are plotted in the quartz-monzonite field in the QAP diagram (Figure 5a) and are plotted in the tholeiitic field in Figure 5c. The A/CNK values range from 0.70 to 0.84, belonging to the metaluminous series (Figure 5d). The contents of SiO_2 = 61.07%–63.60%, of Al_2O_3 = 12.82%–13.79%, of MgO = 1.18%–2.92%, and of TFe_2O_3 = 2.70%–5.18%. LREE is relatively enriched, with La_N/Yb_N ratios ranging from 5.70 to 16.76 (Figure 6). The δEu values vary from 0.75 to 0.84. The ∑REE ranges from 102.70 to 204.60 ppm. In the primitive mantle normalized multi-element plots, almost all samples are enriched in Th, U, Pb, Zr, and Hf and depleted in Rb, Ba, Sr, Nb, Ta, and Ti (Figure 6).

4.2.2. Green Pluton

Gabbro: The majority of samples in green are plotted in the monzogabbro field on the TAS diagram (Figure 5a) and in the potassic field in Figure 5b. The contents of SiO_2 vary from 39.44 to 49.38%, of Al_2O_3 vary from 12.26 to 15.50%, of MgO vary from 4.68 to 10.99%, of TFe_2O_3 vary from 16.04 to 21.35%, and of Mg# vary from 0.53 to 0.71. These

samples show slightly enriched LREE patterns (Figure 6) with moderate negative Eu anomalies (δEu = 0.71–1.12). The ∑REE is 53.27 to 301.86 ppm. The La_N/Yb_N values change from 2.44 to 6.01. On the spider diagram, these rocks are enriched in Rb, K, and Pb and depleted in Sr, Nb, Ta, Zr, Hf, and Ti (Figure 6).

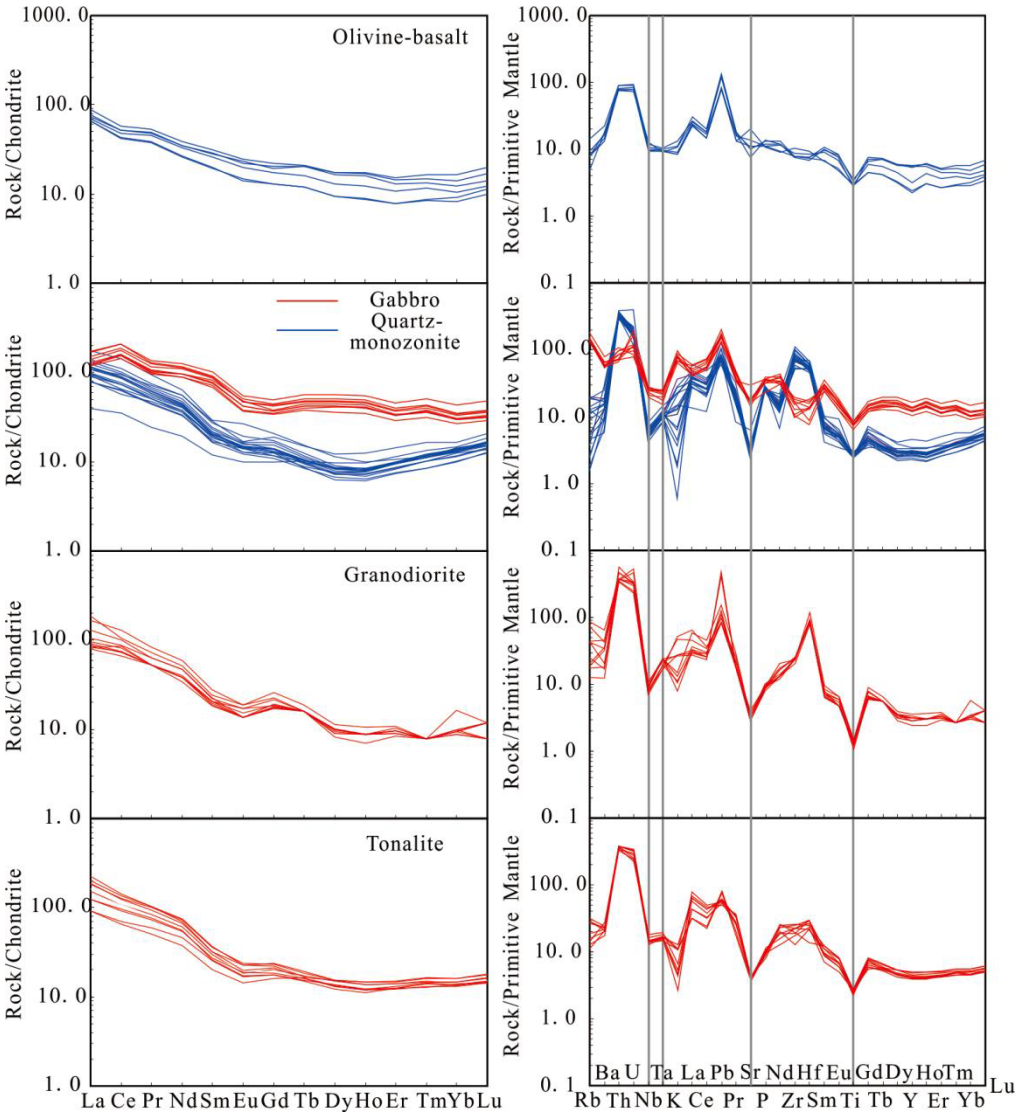

Figure 6. Chondrite-normalized REE patterns and primitive-normalized incompatible element spider diagrams for the magmatic rocks in the southern TSOB. Normalizing values are from [31].

4.3. Whole Rock Sr and Nd Isotopes

The whole-rock Sr and Nd isotopic data of these magmatic rocks are listed in Supplementary Table S3. The initial Sr and Nd isotopic ratios for all these samples were calculated using their crystallized ages. The two-stage Nd mode age (T_{DM2}) can correct the calculation error of the Nd mode age caused by the variation of the Sm/Nd value so that the T_{DM2} relative to the one-stage model ages can better reflect the time when the original magma was differentiated from the mantle reservoir [32,33]. The olivine-basalt displays higher initial $^{87}Sr/^{86}Sr$ ratios ($(^{87}Sr/^{86}Sr)i$) (0.7113–0.7119) and negative εNd(t) values (−4.1 to −2.0), with T_{DM2} varying from 1.40 to 1.57 Ga. The $(^{87}Sr/^{86}Sr)i$ values in the quartz-monzonite range from 0.7122 to 0.7129, and the εNd(t) values vary from −4.2 to −4.5, with T_{DM2} varying from 1.55 to 1.57 Ga. The granodiorite has $(^{87}Sr/^{86}Sr)i$ ratios ranging from 0.7051 to 0.7108 and εNd(t) values ranging from −4.7 to −4.1, with T_{DM2} ranging from 1.52 to 1.59

Ga. The tonalite has ($^{87}Sr/^{86}Sr$)i ratios ranging from 0.7095 to 0.7124 and εNd (t) values ranging from −5.9 to −5.2, with T_{DM2} ranging from 1.57 to 1.62 Ga.

5. Geochronological Framework

Plentiful ages have been obtained through various geochronological methods (such as K-Ar, Ar-Ar, and U-Pb) on granites, gneiss, and gabbro along the TSOB in the last 20 years. However, most of the studies were concentrated on the Indosinian magmatism, whose ages range from 261 to 242 Ma. On the contrary, the age data of the Early Paleozoic magmatism is limited because of the poor outcrop of the magmatic rocks. Shi et al. [6] reported zircon U-Pb ages of ~438 Ma for biotite granite from the Hai Van complex, which is located in the south part of the TSOB. Nakano et al. [18] obtained zircon U-Pb ages of granitic gneiss from the TSOB, whose ages range from 428 to 449 Ma. In the south of the TSOB along the TPSSZ, monazites in schist and zircons in granitic gneiss yield U-Pb ages of 429 Ma and 430 Ma [8]. The contemporaneous magmatism in the TSOB also incorporates the paragneiss (447–452 Ma) of the Kham Duc complex in the Phuoc Son area [21], orthogneiss (407–418 Ma), and granitoid (423–427 Ma) of the Dai loc complex in the west of Da Nang [1,11], and detrital zircons (445–448 Ma) of Paleozoic sedimentary rocks in TSOB [2]. These ages indicate that a major tectono-magmatic event related to the Tethyan orogeny has occurred in this zone. The occurrence of the mafic-ultramafic ophiolitic suite along the TPSSZ can also support this conclusion [6,8,34].

The olivine-basalt from the Awen magmatic complex yields an intrusive age of 507 Ma, which is by far the oldest age in the TSOB. The gabbro from the Green quartz-monzonite and the granodiorite from the Awen magmatic complex have crystallization ages of 478.9–485.6 Ma and 483.3–456.9 Ma, respectively, which are the first discovered magmatic rocks recorded in this stage. Additionally, the tonalite from the Awen magmatic complex has ages of 417–419 Ma, which is consistent with the age of gneiss (407–418 Ma) at the Dai loc complex published by Carter et al. [11]. We have reviewed most of the published ages on the magmatic rocks in TSOB and the adjacent Kontum massif. Up to now, about forty ages were collected in this area. Our new age results, together with these previous ages of different rocks, will constrain the Early Paleozoic magmatism in TSOB and help us to establish the geochronological framework during this period in TSOB.

According to these data, the age distribution histogram of magmatic rocks was made (Figure 7). These rocks are mainly distributed along the EW-trending TPSSZ and the adjacent Kontum terrane. As can be seen in Figure 7, the Early Paleozoic magmatism in the TSOB massif lasted for a long time, with ages ranging from 520 Ma to 360 Ma. The peak age appears in 440–460 Ma, indicating the magmatism in this period is the most intense. This phenomenon is consistent with the tendency of magmatism in the subduction process to increase gradually before the collision, reach a peak in the collision stage, and decrease subsequently in the post-collision stage, as reported by the evolution of the Central Asian orogenic belt [35], the Gangdise magmatism arc in Tibet [36], and the Qinling-Kunlun orogenic belt [37]. Given the above, the Early Paleozoic magmatism might be related to the long process of northward subduction of the Tamky-Phuoc Son Ocean, which has been considered as a branch of the Proto-Tethys Ocean [38]. Moreover, the Early Paleozoic magmatism in the TSOB can be further subdivided into four different stages (~507 Ma, 483–461 Ma; 461–438 Ma; and 438–410 Ma) based on our new geochronological framework (Figure 8). The rock associations in different stages are various. Moreover, multidisciplinary approaches, including stratigraphy, metamorphism, and plate tectonics, supported this conclusion. A detailed elucidation is demonstrated in Section 6.2. These four stages correspond to the specific period of the subduction of the Tamky-Phuoc Son Ocean.

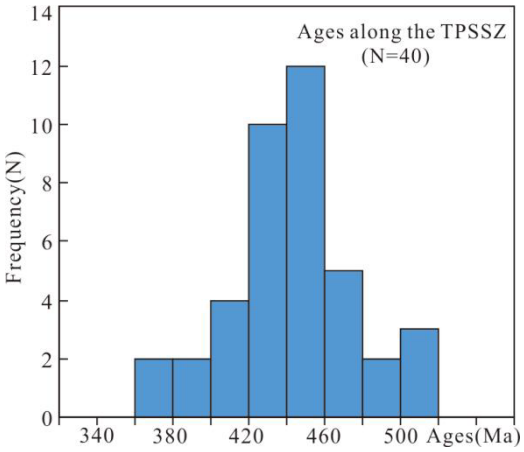

Figure 7. Age distribution of the magmatic rocks on both TSOB and Kontum massif; the ages are listed in Supplementary Table S4.

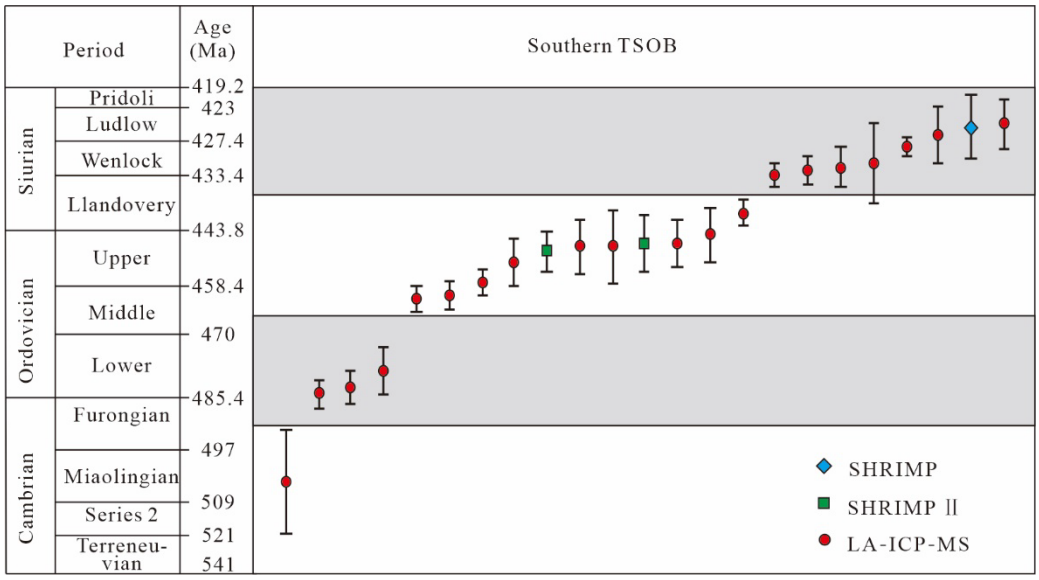

Figure 8. Summary of the Early Paleozoic ages for magmatic rocks along southern TSOB in Laos. Data from [2,6,8,14,21] and this study.

6. Discussion

6.1. Petrogenesis and Magma Source

Magma can be formed through different mechanisms (fractional crystallization or partial melting) in various geodynamic settings [39,40]. The geochemical and isotopic signatures of these magmatic rocks in the southern TSOB were used to assess which petrogenetic mechanism was responsible for the formation of these rocks. The magma source of magmatic rocks in the subduction zone is complex; they can derive from oceanic crust, mantle wedge, and the overlying continental crust [41]. As discussed above, the Early Paleozoic magmatism in TSOB can be subdivided into at least four stages (~507 Ma, 483–461 Ma, 461–438 Ma, and 438–410 Ma), and these rocks are composed of basalt, gabbro, and granitoid.

6.1.1. Middle Cambrian (~507 Ma) Magmatism

Middle Cambrian (~507 Ma) olivine-basalt has characteristics of low SiO_2 (36.81%–42.03%) and high MgO (21.03%–23.14%), Cr (868–1078 ppm), and Ni (709–933 ppm) contents. The geochemical signatures of these samples are similar to those of primitive mantle-derived magma [42]. Generally, the Mg# value of basic rocks is an important symbol

to identify the primitive mantle, which always ranges from 0.68 to 0.75 [43]. The values of Mg# in olivine-basalt samples are 0.72 to 0.74, showing the characteristics of primitive basaltic magma. In addition, these samples have relatively high La/Nb (1.88–2.68) and La/Ba (0.12–0.17) ratios and are plotted in the field of the primitive mantle (Figure 9a) [44]. Likewise, these samples exhibit a trend of primitive mantle series in the diagram of Zr vs. Nb (Figure 9b), and the Zr/Nb (9.31–16.73) ratios are similar to the primitive mantle [30]. The primary magma could be generated by 10%–30% partial melting of lherzolite (spinel: garnet = 50:50) (Figure 9c). There are also Mesoproterozoic crustal materials in the magma source, as can be seen in Figure 9d.

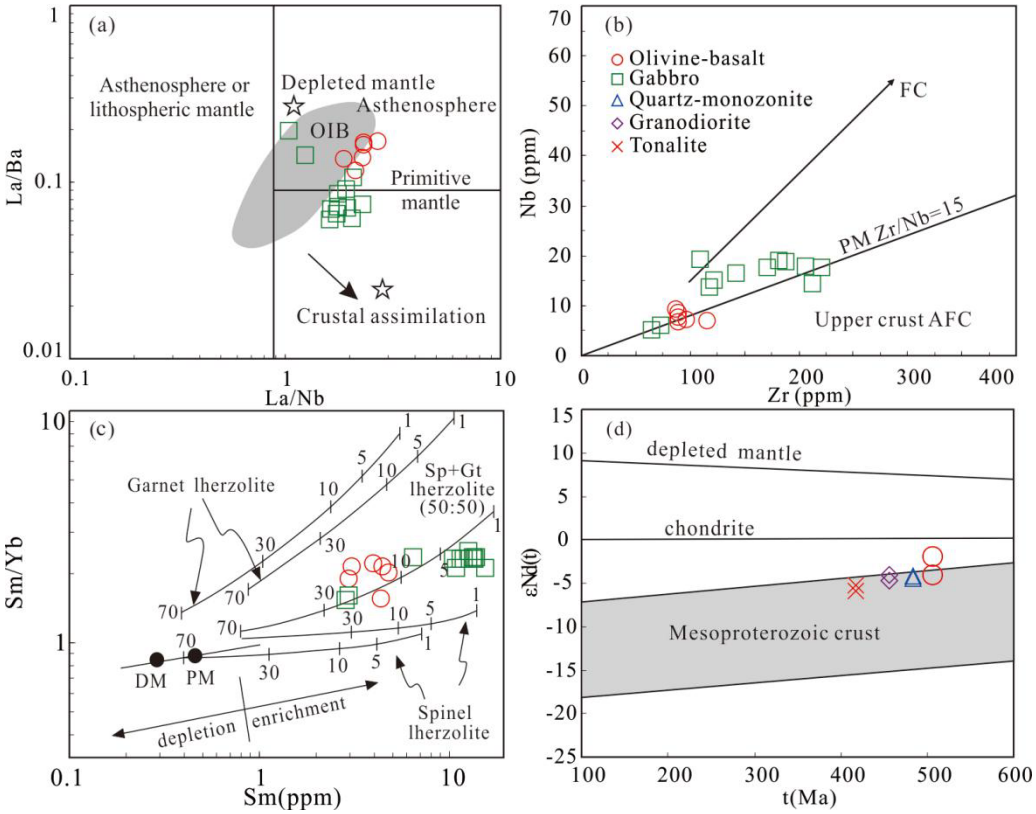

Figure 9. (**a**) La/Nb vs. La/Ba diagram after [45]; (**b**) Zr vs. Nb diagram after [46]; (**c**) Sm vs. Sm/Yb diagram after [47]; and (**d**) t vs. εNd (t) diagram after [48].

The distribution of samples observed in Figure 10 suggests that the olivine-basalt has the EM2 characteristics. The EM2 component may be generated by the metasomatism between the mantle wedge and terrigenous sediments carried by subducted oceanic crust or the fluid derived from the subducted oceanic crust [49,50]. The olivine-basalt is characterized by high ($^{87}Sr/^{86}Sr$)i ratios; negative εNd(t) values; and depletion in Nb, Ta, and Ti in the spider diagram, which shows arc signatures [51] and suggests that these rocks were contaminated by the subducted terrigenous sediments and/or continental crustal materials. These samples exhibit variable Th/Yb ratios and constant Ba/La ratios (Figure 11a), showing the significant addition of terrigenous sediments [52,53]. Furthermore, all these samples are in the field of the mantle wedge, with some extent contamination of terrigenous sediments (Figure 11b) [45]. The Harker diagram (Figure 12) shows that the olivine-basalt exhibits a weak fractional crystallization trend. These selected major and trace elements remain constant, with an increase of the Mg# value. The geochemical characteristics of the olivine-basalt described above indicate that fractional crystallization in the process of magma evolution is insignificant.

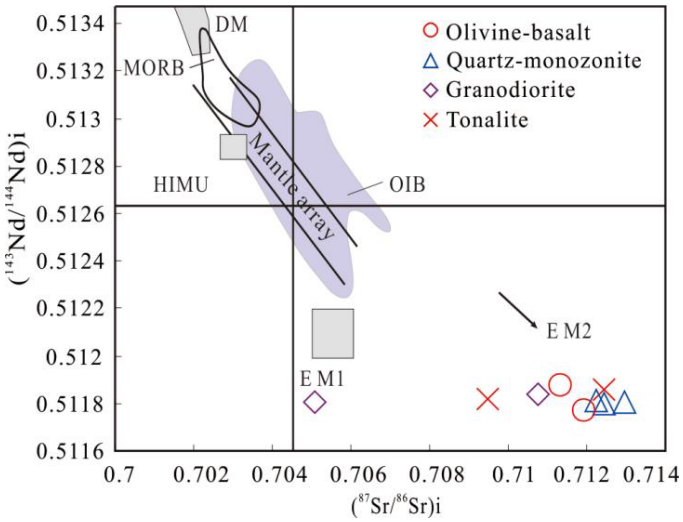

Figure 10. ($^{87}Sr/^{86}Sr$)i vs. ($^{143}Nd/^{144}Nd$)i diagram after [54].

It can be concluded that the olivine-basalt could be generated by the partial melting of the mantle wedge, which has been metasomatized by the terrigenous sediments. The magma was contaminated by minor Mesoproterozoic crustal materials during magma ascent, and the fractional crystallization was limited during the magma evolution.

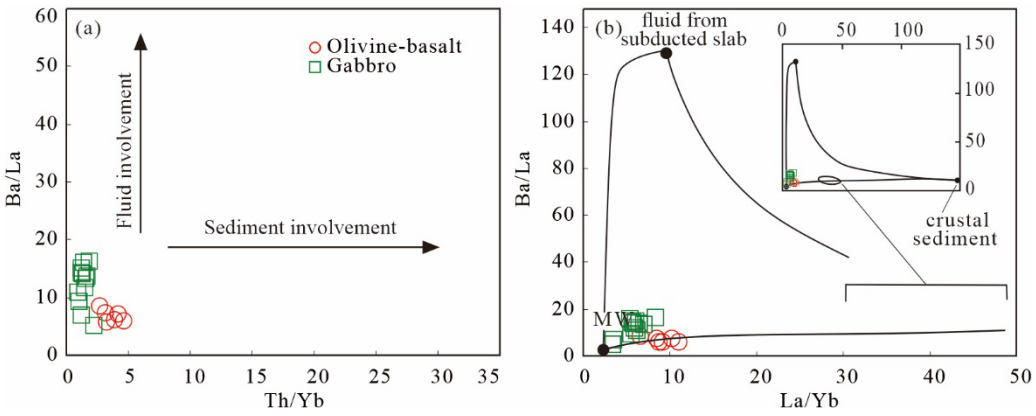

Figure 11. (**a**) Th/Yb vs. Ba/La diagram after [53]; (**b**) La/Yb vs. Ba/La diagram after [44].

6.1.2. Early Ordovician to Middle Ordovician (483–461 Ma) Magmatism

The magmatic rocks in this stage are composed of gabbro in green and quartz-monzonite in Awen. The magma source of gabbro in this stage is primitive mantle, as can be seen in Figure 9a,b. Most of the gabbro samples are distributed in the field of 1%–5% partial melting of lherzolite (spinel: garnet = 50:50) (Figure 9c). The higher K_2O and Na_2O contents, the lower the Cr, Ni, MgO contents, and the Mg# values indicate that the magma has suffered some extent of fractional crystallization because the compatible elements tend to be enriched in the magma evolution. Higher La/Nb ratios and relatively low La/Ba ratios (Figure 9a) show that crustal assimilation in the genesis of these rocks is obvious. Sediments involvement by the subduction of oceanic crust are limited, as can be seen in Figure 11a,b.

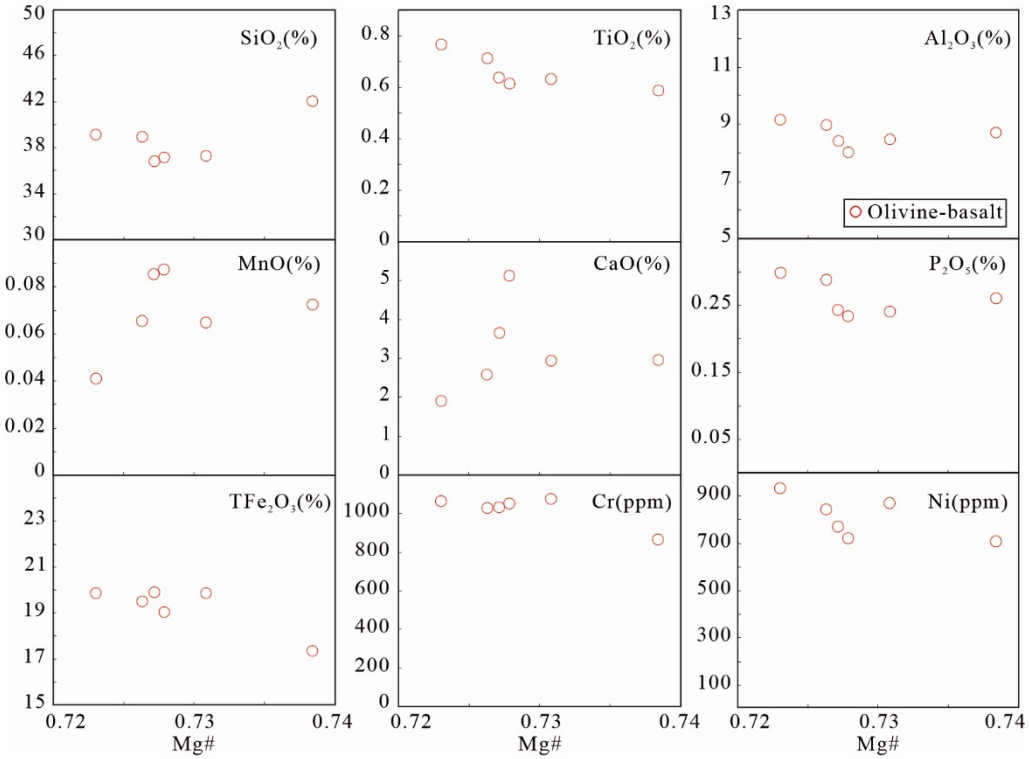

Figure 12. Harker diagrams for olivine-basalt samples.

The quartz-monzonite in Awen has extremely low Sr/Y (3.65–8.79) and (La/Yb)N (2.67–13.68) ratios, which are similar to typical arc-related rocks [55,56]. Generally, the magma formed in arc may derive from the mantle wedge, the subducted oceanic crust, and the lower continent. The quartz monzonite has relatively low SiO_2 (58.5%–65.4%), MgO (1.08%–2.98%), Cr (12.47–24.12 ppm), and Ni (3.42–28.33 ppm) contents; high Na_2O (3.2%–11.5%) content; and high Mg# (0.29–0.42) values. These geochemical signatures are similar to the lower continental crust [57]. The T_{DM2} (1.55–1.57 Ga) of quartz-monzonite shows that the continent component is the Mesoproterozoic lower continental crust. Thus, we propose that the magma source of quartz-monzonite is mainly the lower continental crust. The higher ($^{87}Sr/^{86}Sr$)i (0.7122–0.7129) and negative εNd(t) (−4.2 to −4.5) values show that the enriched magma source or crustal contamination during magma ascend. However, crustal assimilation was negligible during the magma process, which can be supported by the relatively constant ($^{87}Sr/^{86}Sr$)i and εNd(t) values and the change of SiO_2 content. The subducted sediments precipitated fluid- or melt-related metasomatism, which could have resulted in the enriched source region [51]. Fluid has a high migration ability for soluble elements and a poor migration ability for insoluble elements, while aqueous melt has a strong migration ability for all the above elements [58]. The narrow variation range of the Nb/Y ratio indicates the enrichment of subduction fluid, and the wide variation range of the Nb/Y ratio indicates the enrichment of slab-derived melt [59]. The relatively constant Nb/Y ratios (0.21–0.48) in quartz-monzonite indicate that the source enrichment is caused by the fluid metasomatism.

As described above, the magmatism in this stage can be concluded as follows. The basaltic magma was generated by partial melting of the mantle wedge heated by the convecting of the asthenosphere caused by the subduction of the oceanic crust. Subsequently, the basaltic magma intrude and underplate the lower crust and induced partial melting of the lower continental crust and then form the quartz-monzonite.

6.1.3. Late Ordovician to Early Silurian (461–438 Ma) Magmatism

The granodiorite in this stage belongs to the tholeiitic and metaluminous series, with obvious depletion of high field strength element (HFSE), indicating the arc-related magmatic rocks. The involvement of terrigenous sediments in the genesis of magma is obvious, as shown in Figure 11a,b. The terrigenous sediments were dragged into the deeper zone by the subduction of oceanic crust; the fluid was separated out, and then the mantle wedge was metasomatized. Moreover, there was some assimilation of the upper crustal materials during the ascent of magma (Figure 13a,b). These samples have low Nb/Ta (6.10–8.44) and Zr/Hf (7.25–10.79) ratios, which belong to the high differentiated granite in Figure 14a [32]. In addition, based on the partition coefficients of Ba, Sr, and Rb in biotite, hornblende, pyroxene, and feldspar, the trend of mineral crystallization can be further distinguished [60]. As can be seen in Figure 14b–d, the crystallization of hornblende and biotite is notable during the magma evolution. The existence of negative Eu and Sr abnormity indicates the fractional crystallization of plagioclase. The differentiation index of the granodiorite ranged from 76 to 81, showing the characteristics of high differentiation. Additionally, the mineral assemblages have a large crystal size.

The characteristic mineral assemblages in granodiorite are the emergence of biotite (5%). The characteristics of I-type granite (Figure 15a–d) suggest that the magma source is mafic rocks. This phenomenon may be due to the heterogeneous assimilation of sediments and/or the slab derived fluids. Moreover, all samples are plotted in the Mesoproterozoic crustal evolutionary zone in Figure 9d. Combining with the geochemical and mineralogical signatures of these rocks, the magma source of these rocks is mainly composed of the lower Mesoproterozoic continental crust.

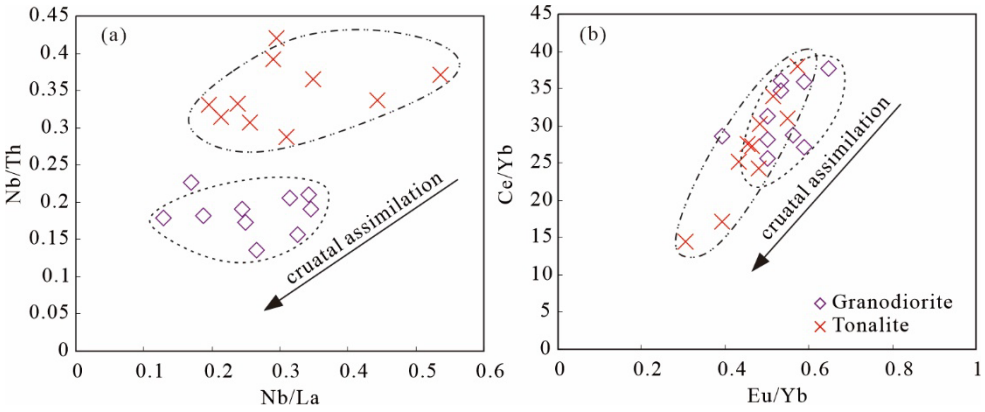

Figure 13. (**a**) Nb/La vs. Nb/Th diagram; (**b**) Eu/Yb vs. Ce/Yb diagram after [61].

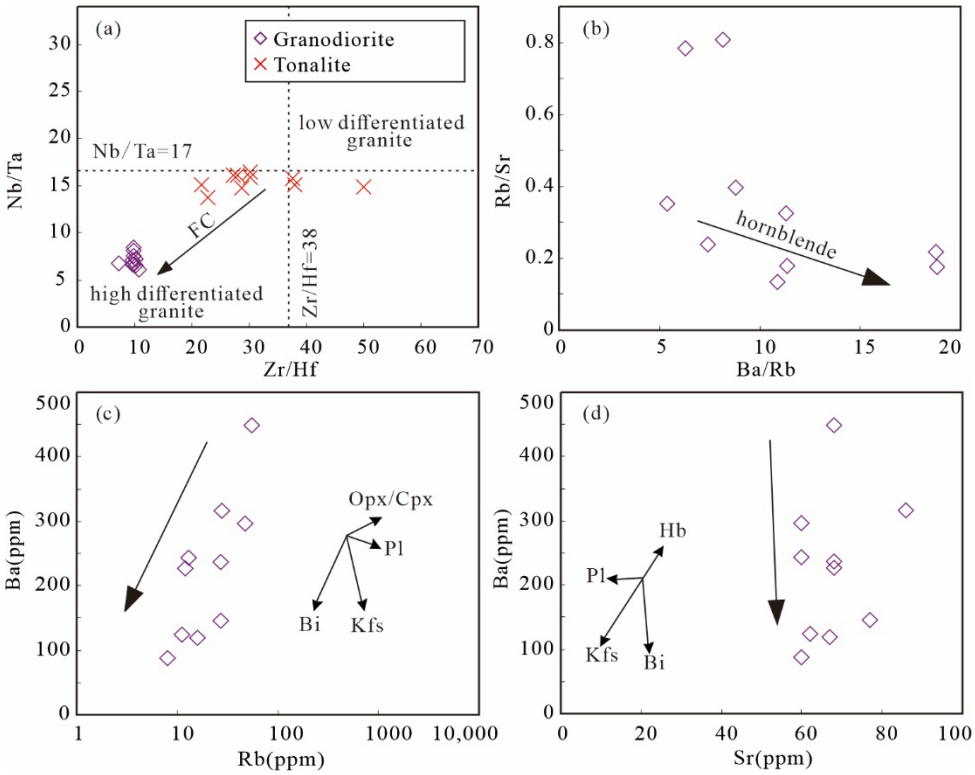

Figure 14. (**a**) Zr/Hf vs. Nb/Ta diagram after [32]; (**b**–**d**) fractional crystallization discrimination diagrams for granodiorite.

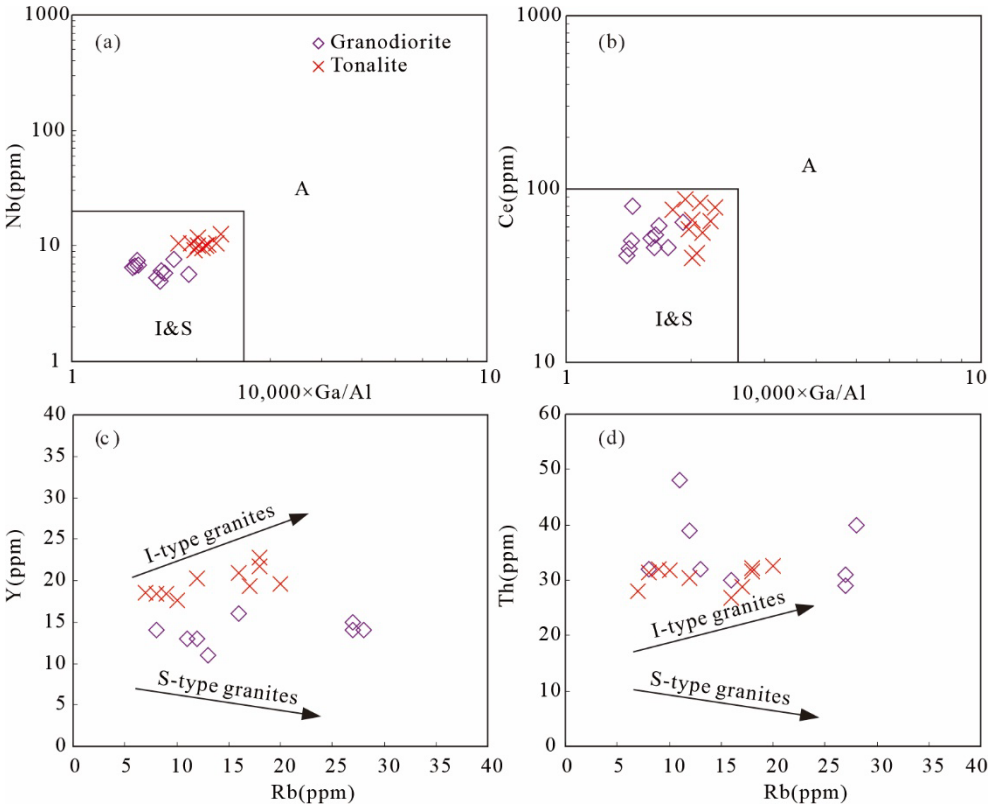

Figure 15. (**a**) 10000×Ga/Al vs. Nb diagram [40]; (**b**) 10000×Ga/Al vs. Ce diagram [40]; (**c**) Rb vs. Y diagram; and (**d**) Rb vs. Th diagram [62].

6.1.4. Early Silurian to Late Silurian (438–410 Ma) Magmatism

The tonalite in this stage contains low MgO (1.18%–2.92%), Cr (10.96–20.54 ppm), and Ni (13.98–34.45 ppm) contents. The A/CNK values range from 0.70 to 0.84, which indicates that these rocks belong to the metaluminous series. This is consistent with the signature of I-type granite revealed by the geochemical diagrams in Figure 15a–d. All of these features suggest that these rocks are geochemically related to the lower continental crust, and the negative εNd(t) (−5.9 to −5.2) and higher ($^{87}Sr/^{86}Sr$)i (0.7095–0.7124) values also favor this conclusion. In addition, all samples exhibit the EM2 trend in Figure 10 showing the characteristics of the lower crust. As described, the magma of these rocks is mainly derived from the partial melting of the lower Mesoproterozoic crust with minor terrigenous sediments (Figure 11a,b). It is crucial to note that although the content of terrigenous sediment is limited, the impact on the geochemical variation in magma is notable. In the process of magma ascent, the assimilation of the upper crustal material is inevitable, as revealed in Figure 13a,b. The high contents of Th (26.9–32.53 ppm) and U (4.19–7.12 ppm) also indicate the assimilation of the upper crust because of the high contents of Th and U in the upper crust [63]. The fractional crystallization is moderate, as shown in Figure 14a. The variation trend of Ba/Rb vs. Rb/Sr (Figure 16a) indicates that hornblende is the major crystallization phase. Likewise, the fractional crystallization of K-feldspar, plagioclase, and biotite can also be identified in Figure 16b–d.

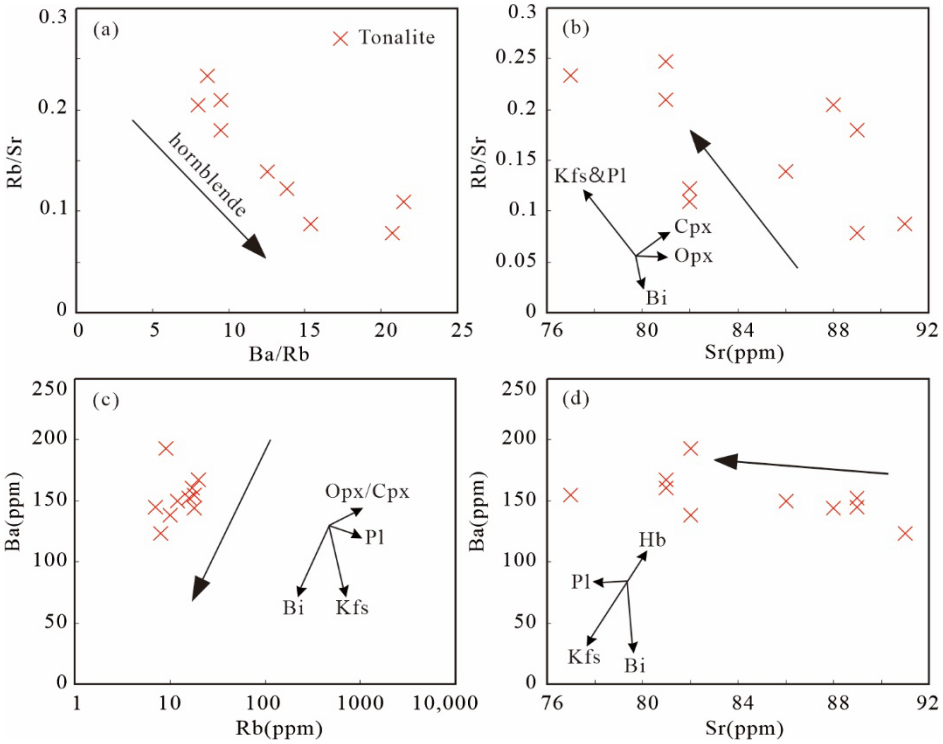

Figure 16. Fractional crystallization discrimination diagrams for tonalite. (**a**) Ba/Rb vs. Rb/Sr diagram; (**b**) Sr vs. Rb/Sr diagram; (**c**) Rb vs. Ba diagram; (**d**) Sr vs. Ba diagram. Bi—biotite; Pl—plagioclase; Kfs—K-feldspar; Hb—hornblende; Cpx—clinopyroxene; and Opx—orthopyroxene.

In summary, slab-originated melts have MORB-like Sr-Nd isotopic compositions, which are similar to those of the subducted oceanic crust [57]. On the contrary, the Early Paleozoic magmatic rocks have more evolved Sr-Nd compositions (Figure 10). The T_{DM2} ranges from 1.40 to 1.62 Ga, indicating that the oceanic crust cannot be the magma source of these rocks. The T_{DM2} also provides a constraint for the Precambrian crustal record of the TSOB, where the Mesoproterozoic basements existed, as illustrated in Figure 9d. Moreover, all these Early Paleozoic magmatic rocks show depletion in HFSE (Nb, Ta, and Ti) and Rb, Ba, and Sr, which can be interpreted as derived from the ancient lower crust

[64]. Low Rb (1–113 ppm) contents and Rb/Sr (0.01–0.81) ratios are consistent with the lower crust [65]. The depletion of Rb may be caused by the granulite facies metamorphism [66]. Although the outcrops of Proterozoic basements are limited to the mainland of Indochina block, there are Proterozoic radioisotopic ages of schists and gneisses in Thailand and Vietnam [67] and Proterozoic detrital zircons in TSOB [2]. Lan et al. [68] also confirmed that the Indochina block was formed in the Proterozoic through the research of the Kontum core complex using Sr-Nd isotopic and geochemical methods. The tholeiitic characteristics of granitoid in TSOB might result from the inheritance of the source rocks. Frost et al. [69] pointed out that the geochemical signatures of granitic rocks are controlled by multiple factors, including the magma source, magma differentiation, and tectonic setting.

6.2. Tectonic Setting and Geodynamics

The timing and geometry of the suture and subsequent collision between the Troung Son terrane and the Kontum Massif have not been fully defined because of the low degree of geological research [70]. The tectonic setting of the Early Paleozoic magmatic rocks in the TSOB is still controversial. After detailed geochemical and isotopic analyses, Nagy et al. [12] and Hutchison [17] proposed that the magmatism in the Early Paleozoic was formed by the split of the Indochina block from Gondwanaland and the northward subduction in Ordovician-Silurian, while Carter et al. [11] thought that the magmatism was related to the extensional tectonics before the breakup of Gondwanaland. Geochronological and petrological evidence has revealed that the intracontinental orogeny of the South China block drove the South Vietnam block (Kontum massif) to subduct beneath the North Vietnam block (Truong Son terrane) and collided at about 460–450 Ma and then formed the TPSSZ [13]. Based on large-scale monazite geochronological and geochemical research of the metamorphic complex in Kontum terrane, Nakano et al. [18] hold the viewpoint that the arc-related magmatism was formed in the active continental margin before the collision between the South China and Indochina block. However, most of the magmatic rocks in the Early-Late Ordovician were covered by the Late Silurian epimetamorphic turbidite. For this reason, there were few magmatic rocks outcropped. As a result, previous studies mainly focused on the research of the outcropped magmatic rocks that formed at a specific geological time in the Early Paleozoic, resulting in their limitation in understanding the tectonic setting of this belt and a scarcity of research on the intact geodynamic evolution of the TSOB in the Early Paleozoic.

The existing data obtained in recent years is of great significance for our understanding of the tectonic setting and geodynamic evolution of the TSOB in the Early Paleozoic. The exploration of the Awen gold district in recent years has disclosed abundant mafic to felsic magmatic rocks. Different kinds of magmatic rocks have been systematically collected and studied. Our new geochronological framework indicates that the geodynamic evolution of the TSOB in Laos can be further subdivided into at least four stages (~507 Ma, 483–461 Ma, 461–438 Ma, and 438–410 Ma). This study firstly confirmed the existence of a magmatic belt in the Cambrian to Early Silurian in the Awen gold district at the southern TSOB. It further verified that the Proto-Tethys Ocean existed in the Late Cambrian and began to subduct beneath the Truong Son terrane at ca.507 Ma. During Late Neoproterozoic-Early Palaeozoic times, the major Asian blocks were composed of South China, North China, Qaidam, Tarim, Indochina, and North Qiangtang. These blocks were separated from the northern margin of Gondwana by the Proto-Tethys [71]. The Proto-Tethys is an archipelagic ocean that includes multiple branches separating micro-continental blocks and arcs [72–74]. The Hiep Duc complex in the TPSSZ contains abundant disjointed serpentinized mafic-ultramafic rocks, which show ophiolitic affinities [8,34]. Tran et al. [8] and Shi et al. [6] further argued that the TPSSZ represents a suture zone of an Early Paleozoic subduction-collision event and is considered to be a remnant of ancient oceanic crust. The detrital zircon and paleontological studies of the TSOB and Kontum massif show that the TSOB was connected to the Indian margin of Gondwana, and the Kontum massif was adjacent to the Australian margin of Gondwana during the early Paleozoic [2,38,75–78].

This difference confirms that the Tamky-Phuoc Son Ocean existed between the TSOB and Kontum terrane during the Early Paleozoic. In this period, the Tamky-Phuoc Son Ocean represents a branch ocean of Proto-Tethys. The Early Palaeozoic ophiolitic rocks and eclogites in the east of the Changning-Menglian Suture zone represent remnants of the Proto-Tethys Ocean, which closed in the Silurian [71,79,80]. The TPSSZ in central Vietnam extended westward to the Awen gold district in Laos, representing the closure of the Tamky-Phuoc Son Ocean, which existed in the Early Paleozoic. After that, the Truong Son terrane and the Kontum massif were connected as a unified continent.

The latest geochronological framework shows that the magmatism in Kontum massif and the magmatism in the southern TSOB have similar evolution characteristics. The Tamky-Phuoc Son Ocean was a bidirectional subduction whose northward subduction beneath the Truong Son terrane with magmatism mainly continued from 507 Ma to 410 Ma and southward subduction beneath the Kontum massif, with magmatism ranging from 518 Ma to 380 Ma in the Early Paleozoic [6,8,12]. During the subduction process, a set of magmatic rock assemblages formed in the island-arc setting with characteristics of depleted HFSE. Finally, combined with previous findings, a tentative model related to the geodynamic evolution of the TSOB in the Early Paleozoic is presented.

The Middle Cambrian (~507 Ma) comprised the early stage of the bidirectional subduction of the Tamky-Phuoc Son Ocean, with northward subduction beneath the Truong Son terrane and southward subduction beneath the Kontum massif. In the diagrams of Hf/3-Th-Ta (Figure 17a) and Ti/100-Zr-Sr/2 (Figure 17b), all these samples are plotted in the field of calc-alkaline basalt, which is consistent with the volcanic arc tectonic setting. The enriched ($^{87}Sr/^{86}Sr$)i (0.7113–0.7119) and negative εNd(t) values (−4.1 to −2.0) of the olivine-basalt also show arc-like features. Moreover, the depletion of Nb, Ta, and Ti and enriched Th and U are consistent with the rocks formed in the arc setting. The magmatic rocks in the Hiep Duc ultramafic-mafic complex in the TPSSZ also show arc-type geochemical features [34,38]. Moreover, the presence of deep-water sedimentary rocks in the TPSSZ suggests that this rock assemblage was probably formed in an oceanic setting [38]. In the Phuoc Son area within the TPSZ, some boninitic rocks were found that are typical rocks in forearcs [81]. All this evidence above together verified that the southern TSOB might result in a forearc or volcanic arc setting. The olivine-basalt with an age of 507 Ma may be a product of the melting of the mantle wedge during the subduction process, which provides strong evidence for the northward subduction beneath the Truong Son terrane of the Tamky-Phuoc Son Ocean, and the subduction began in the Middle Cambrian (Figure 18a). The south-dipping subduction started earlier than the northward subduction, which can be confirmed by the diorite that formed in 520 Ma from the Dieng Bong complex in the northern Kontum massif [38]. However, the date of the initial northward subduction of the Tamky-Phuoc Son Ocean remains unclear, and further studies are needed to reveal it.

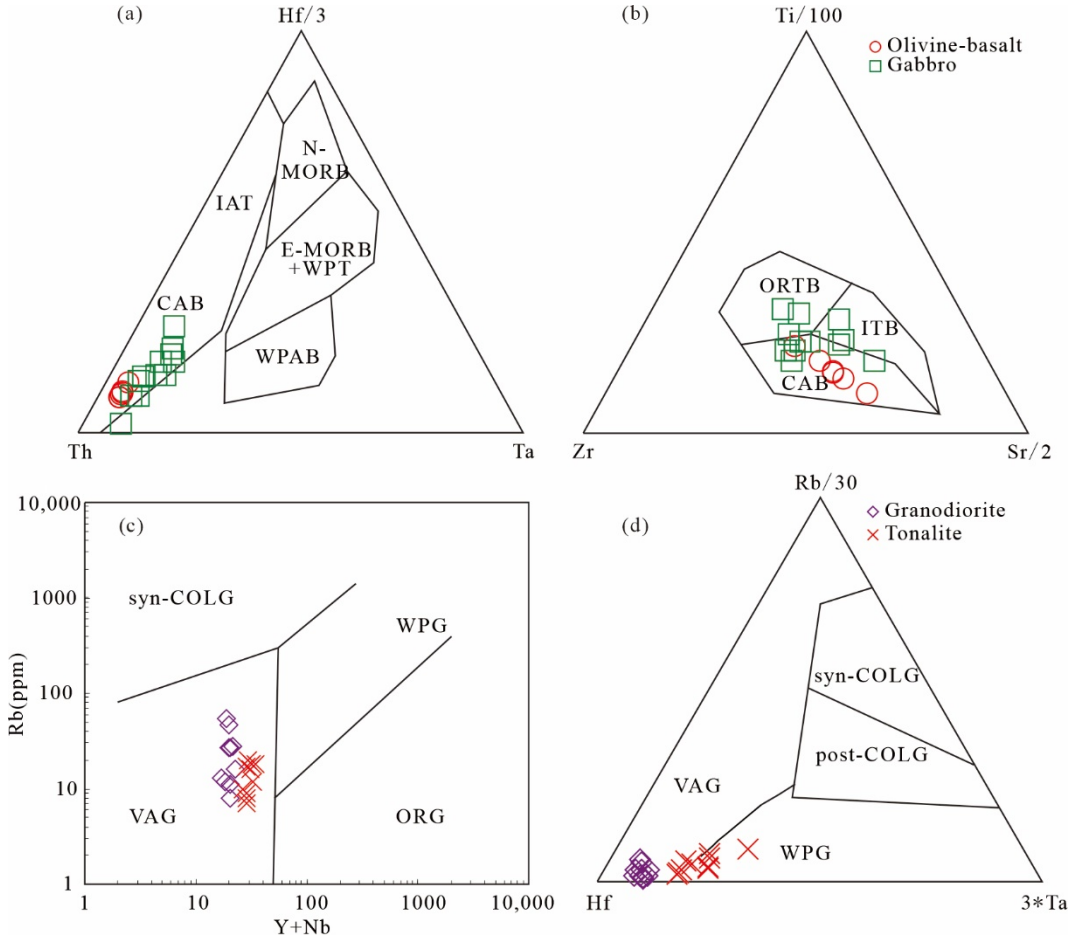

Figure 17. Discrimination diagram for tectonic setting. (**a**) Hf/3-Th-Ta diagram; (**b**) Ti/100-Zr-Sr/2 diagram after [82]; (**c**) Y + Nb vs. Rb diagram after [64]; and (**d**) Rb/30-Hf-3*Ta diagram after [83].

The Early Ordovician-Middle Ordovician (483–461 Ma), the gabbro, and the quartz-monzonite in this stage are characterized by the enrichment of LREE and the depletion of HFSE. Most of the gabbro samples in Figure 17a,b belong to the calc-alkaline basalt. All these signatures indicate that these rocks formed in the active continental margin setting, which is associated with the northward subduction of the Tamky-Phuoc Son Ocean [84–86]. Moreover, the geochemistry and geochronological characteristics of the rhyolitic tuffs and diorites at Donken indicates these rocks were emplaced in an island arc setting during the Early Ordovician (470–476 Ma, [5]). The Donken area is situated near the Po Ko suture zone. The Ordovician strata in south of the TSOB are characterized by a series of deep-water sedimentary rocks. These rocks at the Long Dai Formation are primarily composed of rhythmic alternations of sandstone, siltstone, and mudstone, with intercalations of radiolarian chert, and andesitic layers [13,87,88]. The stratigraphic features, as well as the arc magmatic rock associations discovered in this study, indicate an arc setting. Together with the Ordovician magmatism in the south of the TSOB, we suppose that the Ordovician arc magmatism may be induced by the northward subduction of the Tamky-Phuoc Son Ocean under the Truong Son terrane. The emergence of arc magmatic rock assemblages of gabbro and granitoid, as well as the widespread black slate series, marked the formation of the TSOB and the closure of the Tamky-Phuoc Son Ocean in the Early Ordovician to the Middle Ordovician (Figure 18b).

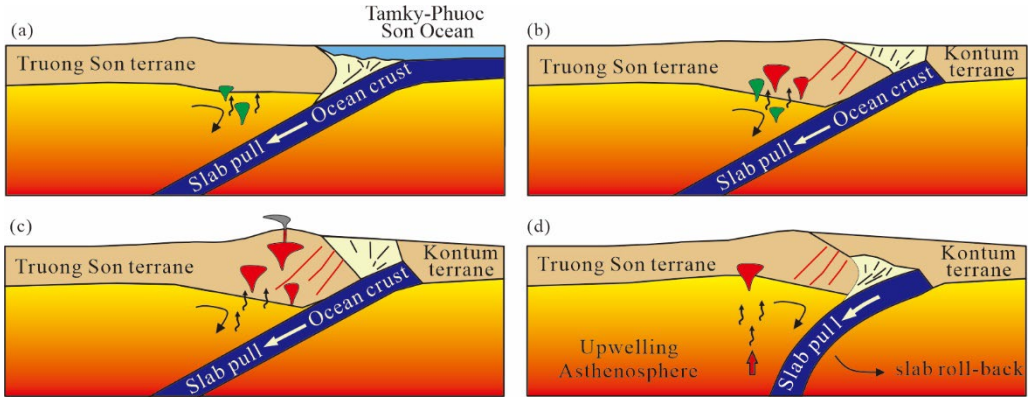

Figure 18. Tectonic evolutionary model of the southern TSOB. (**a**) Middle Cambrian (~507 Ma); (**b**) Early Ordovician-Middle Ordovician (483–461 Ma); (**c**) Middle Ordovician-Early Silurian (461–438 Ma); (**d**) Early Silurian-Early Devonian (438–410 Ma).

In the Middle Ordovician-Early Silurian (461–438 Ma), the tholeiitic I-type granodiorite formed in 457–460 Ma had similar geochemical signatures to subduction-related granitoid in active continental margin settings (Figure 17c,d). Based on the SHRIMP U-Pb dating and REE analyses of zircons of paragneiss from the Kham Duc complex in central Vietnam, Usuki et al. [21] gave the first unequivocal evidence for a crustal-thickening event in the Early Paleozoic in the Indochina block, which has the maximum age of metamorphism at ~450 Ma, representing the age of the onset of the crustal-thickening regime. The presence of greenschist to amphibolite facies metamorphism occurred in the Ordovician-Silurian throughout the Kontum Massif, which indicates a regional metamorphic event [5,8,11,12,21]. The rocks of the Kham Duc complex, located in the north part of the Kontum terrane, reached a maximum pressure at approximately 460 Ma, followed by migmatites at ca 450 Ma. Thus, the Kham Duc complex is considered to be a tectonic mélange formed during a collisional orogeny that subsequently underwent crustal melting, giving rise to the migmatites [13]. The metamorphic rocks with ages of ca. 460–400 Ma and the collision-induced structures along the TPSZ [8,21,89,90] support the viewpoint that the TPO should have been closed before the late Silurian. The Early Paleozoic collision orogeny welded the TSOB and the Kontum terrane [13]. Moreover, this collision event caused significant crustal thickening, tectonic deformation, and subsequent regional metamorphism (Tran et al., 2014). As discussed above, the final suturing event took place at ca. 450 Ma [13,21]. Our research confirms that the pre-Indosinian collisional event was caused by the northward subduction of the Tamky-Phuoc Son Ocean, which eventually collided with the Truong Son terrane at ~450 Ma (Figure 18c).

The Early Silurian-Early Devonian (438–410 Ma) is the late stage of orogeny; the S-type granitoid (423–427 Ma) in the Dai Loc complex was produced by partial melting of metapelites in this stage [13]. The orthogneiss and sericite-feldspar-quartz schist from the Tra Bing complex has ages of 432 Ma and 430 Ma, respectively, which represent the protolith and metamorphic ages [8]. Moreover, the deposits in the Early Silurian are primarily composed of tuffaceous shales and sandstone, without andesitic rocks having been discovered. These rocks were unconformably covered by the Late Silurian Dai Giang Formation (423–419 Ma, [13]). These tonalite samples with arc-like characteristics are plotted in the intersection of the volcanic arc and the within-plate in Figure 17c,d, indicating the transition regime from convergence to back-arc extension. At this stage, the slab retreat, accompanied by asthenosphere upwelling and convection, induced the partial melting of the basement materials and then formed the intermediate-acid magma (Figure 18d). The slab retreat was accompanied by a dextral strike-slip fault and related volcanism in present-day eastern Sicily. Generally, similar to the modern subduction system, the slab retreat can cause a backarc opening, migration of volcanic arcs, the extension of the overriding plate, and accretionary forearc systems [91–94]. However, due to a lack of research in

the TSOB, more detailed studies are needed in further geological works. The above geodynamic scenarios reveal a long-lasting tectonic history of the TSOB in the Early Paleozoic during the Tethyan orogeny. In summary, the TSOB was an independent terrane during the Early Palaeozoic. Geochronological, geochemical, and isotopic signatures of the Early Palaeozoic magmatic rock associations of the southern TSOB indicate that they represent an intact tectono-magmatic evolution of an active continental margin transfer to the passive continental margin about the Truong Son terrane, the Tamky-Phuoc Son Ocean, and the Kontum massif. These scenarios are consistent with observations in the Mediterranean orogenic belts, where the Cenozoic Calabrian subduction system is developed [92].

7. Conclusions

Based on geochemical, isotopic, and geochronological data of the Early Paleozoic magmatic rocks in the southern TSOB, we draw the following conclusions.

(1) Our ages present a new geochronological framework of magmatism along the TSOB in Laos. Four stages (~507 Ma, 483–461 Ma, 461–438 Ma, and 438–410 Ma) of the geodynamic evolution of the TSOB are responsible for the generation of different kinds of magmatic rocks in the Early Paleozoic.
(2) The mafic rocks belong to the potassic series and are mainly generated by the partial melting of the mantle wedge, and the tholeiitic I-type granitoid is derived from the melting of the lower Mesoproterozoic continental crust. Both the gabbro and granitoid have arc signatures were depleted in Nb, Ta, and Ti. These rocks are related to the northward subduction of the Tamky-Phuoc Son Ocean.
(3) The Middle Cambrian (~507 Ma) is the early stage of the bidirectional subduction of the Tamky-Phuoc Son Ocean, with northward subduction beneath the Truong Son terrane and southward subduction beneath the Kontum massif. The Early Ordovician to Middle Ordovician (483–461 Ma) is the main subduction stage of the Tamky-Phuoc Son Ocean, and the Tamky-Phuoc Son Ocean is closed in this stage. The Late Ordovician to Early Silurian (461–438 Ma) is the collision stage of the Tamky-Phuoc Son Ocean and Truong Son terrane. The Early Silurian to Late Silurian (438–410 Ma) is the late stage of collision with the slab roll-back.

Supplementary Materials: The following supporting information can be downloaded at: https://www.mdpi.com/article/10.3390/min12080923/s1, Supplementary Table S1: Zircon U-Pb isotopic data obtained by LA-ICP-MS for the magmatic rocks from the southern TSOB, Laos; Supplementary Table S2: Whole-rock geochemical data of the magmatic rocks from the southern TSOB, Laos; Supplementary Table S3: Sr and Nd isotopic data for the magmatic rocks from the southern TSOB, Laos; and Supplementary Table S4: Ages from the southern TSOB in Laos and the Kontum Massif in Vietnam.

Author Contributions: Conceptualization, Y.C. and Z.S.; methodology, Y.C.; validation, Z.S.; formal analysis, Z.S.; investigation, Y.C. and Z.S.; resources, Y.C.; data curation, Z.S.; writing—original draft preparation, Z.S.; writing—review and editing, Y.C. and Z.S.; visualization, Z.S.; supervision, Y.C.; project administration, Y.C.; and funding acquisition, Y.C. All authors have read and agreed to the published version of the manuscript.

Funding: This research was funded by National Natural Science Foundation of China (grant Nos: 41972312 and 41672329) and the National Key Research and Development Project of China (No: 2016YFC0600509).

Data Availability Statement: The data presented in this study are available in Supplementary Tables S1–S4.

Acknowledgments: We are thankful to Biao Zhang, Zhengshang Liu, Huan Li, and Jin Xie for their assistance with the collection of samples, and Shibo Liu for his help with zircon U–Pb dating. We also sincerely thank the editor and the anonymous reviewers for providing insightful comments for improving the manuscript.

Conflicts of Interest: The authors declare no conflict of interest.

References

1. Hieu, P.T.; Dung, N.T.; Thuy, N.T.B.; Minh, N.T.; Minh, P. U–Pb ages and Hf isotopic composition of zircon and bulk rock geochemistry of the Dai Loc granitoid complex in Kontum massif: Implications for early Paleozoic crustal evolution in Central Vietnam. *J. Mineral. Petrol. Sci.* **2016**, *111*, 326–336.
2. Wang, C.; Liang, X.Q.; David, A.F.; Fu, J.G.; Jiang, Y.; Dong, C.G.; Zhou, Y.; Shunv Wen, S.N.; Phan, V.Q. Detrital zircon U-Pb geochronology, Lu-Hf isotopes and REE geochemistry constrains on the provenance and tectonic setting of Indochina Block in the Paleozoic. *Tectonophysics* **2016**, *677*, 125–134.
3. Zaw, K.; Meffre, S.; Lai, C.-K.; Burrett, C.; Santosh, M.; Graham, I.; Manaka, T.; Salam, A.; Kamvong, T.; Cromie, P. Tectonics and metallogeny of mainland Southeast Asia—A review and contribution. *Gondwana Res.* **2013**, *26*, 5–30.
4. Chen, Y.Q.; Liu, J.L.; Feng, Q.L.; Huang, J.N.; Zhang, H.Y.; Liu, H.G.; Zhao, H.J. *Tectonic Setting and Tectono-Magmatic Evolution: Geology and Granite-Related Deposits in Indochina Peninsula, Southeast Asia*; Geological Publishing House: Beijing, China, 2010; pp. 46–75. (In Chinese with English Abstract)
5. Gardner, C.; Graham, I.; Belousova, E.; Booth, G.; Greig, A. Evidence for Ordovician subduction-related magmatism in the Truong Son terrane, SE Laos: Implications for Gondwana evolution and porphyry Cu exploration potential in SE Asia. *Gondwana Res.* **2017**, *44*, 139–156.
6. Shi, M.F.; Lin, F.C.; Fan, W.Y.; Deng, Q.; Cong, F.; Tran, M.D.; Zhu, H.; Wang, H. Zircon U-Pb ages and geochemistry of granitoids in the Truong Son terrane, Vietnam: Tectonic and metallogenic implications. *J. Asian Earth Sci.* **2015**, *101*, 101–120.
7. Manaka, T.; Zaw, K.; Meffre, S.; Vasconcelos, P.; Golding, S.; Cairns, C. Geology, geochronology and geochemistry of the Ban Houayxai epithermal Au-Ag deposit in the Northern Lao PDR: Relationship to the Early Permian magmatism of the Truong Son Fold belt. *Gondwana Res.* **2014**, *26*, 185–197.
8. Tran, H.T.; Zaw, K.; Halpin, J.; Manaka, T.; Meffre, S.; Lai, C.K.; Lee, Y.J.; Le, V.H.; Dinh, S. The Tamky-Phuoc Son Shear Zone in Central Vietnam: Tectonic and metallogenic implications. *Gondwana Res.* **2014**, *26*, 144–164.
9. Sanematsu, K.; Murakami, H.; Duangsurigna, S.; Vilayhack, S.; Duncan, R.A.; Watanabe, Y. 40Ar/39Ar ages of granitoids from the Truong Son fold belt and Kontum massif in Laos. *J. Mineral. Petrol. Sci.* **2011**, *106*, 13–25.
10. Hoa, T.T.; Anh, T.T.; Phuong, N.T.; Pham, T.D.; Tran, V.A.; Izokh, A.E.; Borisenko, A.S.; Lan, C.Y.; Chung, S.L.; Lo, C.H. Permo-Triassic intermediate-felsic magmatism of the Truong Son belt, eastern margin of Indochina. *Comptes Rendus Geosci.* **2008**, *340*, 112–126.
11. Carter, A.; Roques, D.; Bristow, C.; Kinny, P. Understanding Mesozoic accretion in Southeast Asia: Significance of Triassic thermotectonism (Indosinian orogeny) in Vietnam. *Geology* **2001**, *29*, 211–214.
12. Nagy, E.A.; Maluski, H.; Lepvrier, C.; Schärer, U.; Phan, T.T.; Leyreloup, A.; Vu, V.T. Geodynamic significance of the Kontum massif in Central Vietnam: Composite 40Ar/39Ar and U/Pb ages from Paleozoic to Triassic. *J. Geol.* **2001**, *109*, 755–770.
13. Faure, M.; Nguyen, V.V.; Hoaib, L.T.T.; Lepvrierc, C. Early Paleozoic or Early-Middle Triassic collision between the South China and Indochina Blocks: The controversy resolved? Structural insights from the Kon Tum massif (Central Vietnam). *J. Asian Earth Sci.* **2018**, *166*, 162–180.
14. Metcalfe, I. *Palaeozoic-Mesozoic History of SE Asia*; Hall, R., Cottam, M., Wilson, M., Eds.; The SE Asian Gateway: History and Tectonics of Australia-Asia Collision; Geological Society of London Special Publications: Bath, UK, 2011; Volume 355, pp. 7–35.
15. Metcalfe, I. Tectonic framework and Phanerozoic evolution of Sundaland. *Gondwana Res.* **2011**, *19*, 3–21.
16. Metcalfe, I. Palaeozoic and Mesozoic tectonic evolution and palaeogeography of East Asian crustal fragments: The Korean Peninsula in context. *Gondwana Res.* **2006**, *9*, 24–46.
17. Hutchison, C.S. *Geological Evolution of Southeast Asia*; Clarendon: Oxford, UK, 1989; pp. 1–368.
18. Nakano, N.; Osanai, Y.; Owada, M.; Nam, T.N.; Charusiri, P.; Khamphavong, K. Tectonic evolution of high-grade metamorphic terranes in central Vietnam: Constraints from large-scale monazite geochronology. *J. Southeast Asian Earth Sci.* **2013**, *73*, 520–539.
19. Findlay, R.H.; Trinh, P.T. The Structural Setting of the Song Ma Region, Vietnam and the Indochina-South China Plate Boundary Problem. *Gondwana Res.* **1997**, *1*, 11–33.
20. Liu, J.L.; Tran, M.D.; Tang, Y.; Nguyen, Q.L.; Tran, T.H.; Wu, W.B.; Chen, J.F.; Zhang, Z.C.; Zhao, Z.D. Permo-Triassic granitoids in the northern part of the Truong Son belt, NW Vietnam: Geochronology, geochemistry and tectonic implications. G*ondwana Res.* **2012**, *22*, 628–644.
21. Usuki, T.; Lan, C.Y.; Yui, T.F.; Iizuka, Y.; Van Tich Vu, V.T.; Tran, T.A.; Okamoto, K.; Wooden, J.L.; Liou, J.G. Early Paleozoic medium-pressure metamorphism in central Vietnam: Evidence from SHRIMP U-Pb zircon ages. *J. Geosci.* **2009**, *13*, 245–256.
22. Jackson, S.E.; Pearson, N.J.; Griffin, W.L.; Belousova, E.A. The application of laser ablation-inductively coupled plasma-mass spectrometry to in situ U–Pb zircon geochronology. *Chem. Geol.* **2004**, *211*, 47–69.
23. Wiedenbeck, M.; Hanchar, J.M.; Peck, W.H.; Sylvester, P.J. Further characterisation of the 91500 zircon crystal. *Geostand. Geoanal. Res.* **2004**, *28*, 9–39.
24. Liu, Y.; Gao, S.; Hu, Z.; Gao, C.; Zong, K.; Wang, D. Continental and Oceanic Crust Recycling-induced Melt-Peridotite Interactions in the Trans-North China Orogen: U-Pb Dating, Hf Isotopes and Trace Elements in Zircons from Mantle Xenoliths. *J. Pet.* **2009**, *51*, 537–571.
25. Ludwig, K.R. *ISOPLOT 3.00: A Geochronological Toolkit for Microsoft Excel*; Berkeley Geochronology Center: Berkeley, CA, USA, 2003

26. Yan, Q.; Wang, Z.; Liu, S.; Li, Q.; Zhang, H.; Wang, T.; Liu, D.; Shi, Y.; Jian, P.; Wang, J.; et al. Opening of the Tethys in southwest China and its significance to the breakup of East Gondwanaland in late Paleozoic: Evidence from SHRIMP U-Pb zircon analyses for the Garzê ophiolite block. *Chin. Sci. Bull.* **2005**, *50*, 256–264.
27. Streckeisen, A. To each plutonic rock its proper name. *Earth-Sci. Rev.* **1976**, *12*, 1–33.
28. Middlemost, E.A.K. Naming materials in the magma/igneous rock system. *Earth-Sci. Rev.* **1994**, *37*, 215–224.
29. Winchester, J.A.; Floyd, P.A. Geochemical discrimination of different magma series and their differentiation products using immobile elements. *Chem. Geol.* **1977**, *20*, 325–343.
30. Shand, S.J. *Eruptive Rocks*; Thomas Murby & Co.: London, UK, 1927
31. Sun, S.S.; McDonough, W.E. *Chemical and Isotopic Systematics of Oceanic Basalts: Implications for Mantle Composition and Processes*; Saunders, A.D., Norry, M.J., Eds.; Magmatism in the Ocean Basins: Geological Society of London, Special Publication: London, UK, 1989; pp. 13–345.
32. Wu, F.Y.; Liu, X.C.; Ji, W.Q.; Wang, J.M.; Yang, L. Identification and study of highly differentiated granite. *Sci. Sin. (Terrae*) **2017**, *47*, 745–765. (In Chinese)
33. Wang, D.Z.; Shen, W.Z. Genesis of granitoids and crustal evolution in southeast China. *Earth Sci. Front.* **2003**, *10*, 209–220. (In Chinese with English abstract)
34. Izokh, A.E.; Tran, T.H.; Ngo, T.P.; Tran, Q.H. Ophiolite ultramafic-mafic associations in the northern structure of the KonTum block (central Vietnam). *J. Geol. Hanoi* **2006**, *28*, 20–26.
35. Şengör, A.M.C.; Natal'in, B.A. *Paleotectonics of Asia: Fragments of a Synthesis*; Yin, A., Harrison, T.M., Eds.; The Tectonic Evolution of Asia: Cambridge University Press: New York, NY, USA, 1996; pp. 486–640.
36. Zhu, D.C.; Pan, G.T.; Wang, L.Q.; Mo, X.X.; Zhao, Z.D.; Zhou, C.Y.; Liao, Z.L.; Dong, G.C.; Yuan, S.H. Tempo-spatial variations of Mesozoic magmatic rocks in the Gangdise belt, Tibet, China, with a discussion of geodynamic setting- related issues. *Geol. Bull. China* **2008**, *27*, 1535–1550. (In Chinese)
37. Xiao, Q.H.; Wang, T.; Deng, J.F.; Mo, X.X.; Lu, X.X.; Hong, D.W.; Xie, C.F.; Luo, Z.H.; Qiu, R.Z.; Wang, X.X. *Granitoids and Continent Growth of Key Orogens in China*; Geological Publishing House: Beijing, China, 2009; pp. 300–497. (In Chinese)
38. Nguyen, Q.M.; Feng, Q.L.; Zi, J.W.; Zhao, T.Y.; Tran, H.T.; Ngo, T.X.; Tran, D.M.; Nguyen, H.Q. Cambrian intra-oceanic arc trondhjemite and tonalite in the TamKy-Phuoc Son Suture Zone, central Vietnam: Implications for the early Paleozoic assembly of the Indochina Block. *Gondwana Res.* **2019**, *70*, 151–170.
39. Litvinovsky, A.A.; Jahn, B.M.; Zanvilevich, A.N.; Saunders, A.; Poulain, S.; Kuzmin, D.V.; Reichow, M.K.; Titov, A.V. Petrogenesis of syenite-granite suites from the Bryansky Complex (Transbaikalia, Russia): Implications for the origin of A-type granitoid magmas. *Chem. Geol.* **2002**, *189*, 105–133.
40. Whalen, J.B.; Currie, K.L.; Chappell, B.W. A type granites: Geochemical characteristics, discrimination and petrogenesis. *Contrib. Mineral. Petrol.* **1987**, *95*, 407–419.
41. Deng, J.F.; Luo, Z.H.; Su, S.G.; Mo, X.X.; Yu, B.S.; Lai, Y.X.; Zhan, H.W. *Petrgenesis, Tectonic Setting and Mineralization*; Geological Publishing House: Beijing, China, 2004; pp. 1–381. (In Chinese)
42. Frey, F.A.; Prinz, M. Ultramac inclusions from San Carlos, Arizona: Petrologic and geochemical data bearing on their petrogenesis. *Earth Planet. Sci. Lett.* **1978**, *38*, 129–176.
43. Green, D.H. Experimental melting studies on a model upper mantle composition at high pressure under water-saturated and water-undersaturated condition. *Earth Planet. Sci. Lett.* **1973**, *19*, 37–53.
44. Saunders, A.D.; Storey, M.; Kent, R.W.; Norry, M.J. *Consequences of Plume Lithosphere Interactions, Magmatism and the Cause of Continental Breakup*; Storey, B.C., Alabaster, T., Pankhurst, R.J., Eds.; Magmatism and the Causes of Continental Break-Up; Geological Society of London Special Publication: London, UK, 1992; pp. 41–60.
45. Castillo, P.R.; Janney, P.E.; Solidum, R.U. Petrology and geochemistry of Camiguin Island, southern Philippines: Insights to the source of adakites and other lavas in a complex arc setting. *Contrib. Miner. Pet.* **1999**, *134*, 33–51.
46. Derakhshi, M.; Ghasemi, H.; Miao, L.C. Geochemistry and petrogenesis of Soltan Maidan basalts (E Alborz, Iran): Implications for asthenosphere -lithosphere interaction and rifting along the N margin of Gondwana. *Chem. Der Erde* **2017**, *77*, 131–145.
47. Qi, L.; Zhou, M.F. Platinum-group elemental and Sr-Nd-Os isotopic geochemistry of Permian Emeishan flood basalts in Guizhou Province, SW China. *Chem. Geol.* **2008**, *248*, 83–103.
48. Xu, X.S.; Lu, W.M.; He, Z.Y. The age and genesis of Fogang granitic basement and Wushi diorite-gabbro. *Sci. Sin. (Terrae)* **2007**, *37*, 27–38. (In Chinese)
49. Li, S.G. Implications of εNd-La/Nb, Ba/Nb, Nb/Th diagrams to mantle heterogeneity: Classification of island arc basalts and decomposition of EM2 component. *Geochimica* **1994**, *23*, 105–114. (In Chinese with English abstract)
50. Hart, S.R. Heterogeneous mantle domains: signatures, genesis and mixing chronologies. *Earth Planet. Sci. Lett.* **1988**, *90*, 273–296.
51. Liu, H.; Huang, Q.; Uysal, I.T.; Cai, Z.; Wan, Z.; Xia, B.; Zheng, H.; Yang, P. Geodynamics of the divergent double subduction along the Bangong-Nujiang tethyan suture zone: Insights from late Mesozoic intermediate-mafic rocks in central Tibet. *Gondwana Res.* 2020, 79, 233e247.
52. Fu, D.; Huang, B.; Peng, S.B.; Kusky, T.M.; Zhou, W.X.; Ge, M.C. Geochronology and geochemistry of late carboniferous volcanic rocks from northern Inner Mongolia, North China: Petrogenesis and tectonic implications. *Gondwana Res.* **2016**, *36*, 545–560.
53. Woodhead, J.D.; Hergt, J.M.; Davidson, J.P.; Eggins, S.M. Hafnium isotope evidence for 'conservative' element mobility during subduction zone processes. *Earth Planet. Sci. Lett.* **2001**, *192*, 331–346.

54. Fazlnia, A. Origin and magmatic evolution of the Quaternary syn-collision alkali basalts and related rocks from Salmas, northwestern Iran. *Lithos* **2019**, *344–345*, 297–310.
55. Martin, H. Adakitic magmas: Modern analogues of Archaean granitoids. *Lithos* **1999**, *46*, 411–429.
56. Defant, M.J.; Drummond, M.S. Derivation of some modern arc magmas by melting of young subducted lithosphere. *Nature* **1990**, *347*, 662–665.
57. Gao, S.; Rudnick, R.L.; Yuan, H.L.; Liu, X.M.; Liu, Y.S.; Xu, W.L.; Ling, W.L.; Ayers, J.; Wang, X.C.; Wang, Q.H. Recycling lower continental crust in the North China craton. *Nature* **2004**, *432*, 892–897.
58. Zheng, Y.F. Metamorphic chemical geodynamics in continental subduction zones. *Chem. Geol.* **2012**, *328*, 5–48.
59. Kepezhinskas, P.; McDermott, F.; Defant, M.J.; Hochstaedter, A.; Drummond, M.S.; Hawkesworth, C.J.; Koloskov, A.; Maury, R.C.; Bellon, H. Trace element and Sr-Nd-Pb isotopic constraints on a three-component model of Kamchatka arc petrogenesis. *Geochim. Et Cosmochim. Acta* **1997**, *61*, 577–600.
60. Hanson, G.N. The application of trace elements to the petrogenesis of igneous rocks of granitic composition. *Earth Planet. Sci. Lett.* **1978**, *38*, 26–43.
61. Hart, S.R.; Allegre, C.J. *Trace Element Constraints on Magma Genesis*; Hargraves, R.B., Ed.; Physics of Magmatic Processes; Princeton University Press: Princeton, NJ, USA, 1980; pp. 122–152.
62. Chappell, B. Aluminium saturation in I- and S-type granites and the characterization of fractionated haplogranites. *Lithos* **1999**, *46*, 535–551.
63. Rudnick, R.; Fountain, D.M. Nature and composition of the continental crust: A lower crustal perspective. *Rev. Geophys.* **1995**, *33*, 267–309.
64. Pearce, J. Sources and settings of granitic rocks. *Episodes* **1996**, *19*, 120–125.
65. Taylor, S.R.; McLennan, S.M. *The Continental Crust: Its Composition and Evolution*; Blackwell: Oxford, UK, 1985; p. 321.
66. Rudnick, R.L. *Xenoliths-Samples of the Lower Continental Crust*; Fountain, D., Arculus, R., Kay, R.W., Eds.; Continental Lower Crust; Elsevier: Amsterdam, The Netherlands, 1992, pp. 269–316.
67. Metcalfe, I. Gondwana dispersion and Asian accretion: Tectonic and palaeogeographic evolution of eastern Tethys. *J. Southeast Asian Earth Sci.* **2013**, *66*, 1–33.
68. Lan, C.Y.; Chung, S.L.; Long, T.V.; Lo, C.H.; Lee, T.Y.; Mertzman, S.A.; Shen, J.S. Geochemical and Sr-Nd isotopic constraints from the Kontum massif, central Vietnam on the crustal evolution of the Indochina block. *Precambrian Res.* **2003**, *122*, 7–27.
69. Frost, B.R.; Barnes, C.G.; Collins, W.J.; Arculus, R.J.; Ellis, D.J.; Frost, C.D. A Geochemical Classification for Granitic Rocks. *J. Pet.* **2001**, *42*, 2033–2048.
70. Lepvrier, C.; Maluski, H.; Van Tich, V.; Leyreloup, A.; Thi, P.T.; Van Vuong, N. The Early Triassic Indosinian orogeny in Vietnam (Truong Son Belt and Kontum Massif); implications for the geodynamic evolution of Indochina. *Tectonophysics* **2004**, *393*, 87–118.
71. Metcalfe, I. Multiple Tethyan ocean basins and orogenic belts in Asia. *Gondwana Res.* **2021**, *100*, 87–130.
72. Bian, Q.; Gao, S.; Li, D.; Ye, Z.; Chang, C.; Luo, X. A study of the Kunlun-Qilian-Qinling suture system. *Acta Geol. Sin*. **2001**, *75*, 364–374.
73. Yu, M.; Dick, J.M.; Feng, C.; Li, B.; Wang, H. The tectonic evolution of the East Kunlun Orogen, northern Tibetan Plateau: A critical review with an integrated geodynamic model. *J. Asian Earth Sci*. **2020**, *191*, 104168.
74. Liu, Q.; Zhao, G.; Li, J.; Yao, J.; Han, Y.; Wang, P.; Tsunogae, T. Provenance of early Paleozoic sedimentary rocks in the Altyn Tagh orogen: Insights into the paleoposition of the Tarim craton in northern Gondwana associated with final closure of the Proto–Tethys Ocean. *GSA Bull.* **2020**, *133*, 505–522.
75. Usuki, T.; Lan, C.-Y.; Wang, K.-L.; Chiu, H.-Y. Linking the Indochina block and Gondwana during the Early Paleozoic: Evidence from U–Pb ages and Hf isotopes of detrital zircons. *Tectonophysics* **2012**, *586*, 145–159.
76. Burrett, C.; Zaw, K.; Meffre, S.; Lai, C.K.; Khositanont, S.; Chaodumrong, P.; Udchachon, M.; Ekins, S.; Halpin, J. The configuration of Greater Gondwana–evidence from LA ICPMS, U–Pb geochronology of detrital zircons from the Paleozoic and Mesozoic of Southeast Asia and China. *Gondwana Res.* **2014**, *26*, 31–51.
77. Fortey, R.A.; Cocks, L.R.M. *Biogeography and Palaeogeography of the Sibumasu Terrane in the Ordovician: A Review*; Hall, R., Holloway, J.D., Eds.; Biogeography and Geological Evolution of SE Asia; Backhuys Publishers: Leiden, The Netherlands, 1998; pp. 43–56.
78. Zhu, D.C.; Zhao, Z.D.; Niu, Y.; Dilek, Y.; Mo, X.X. Lhasa terrane in southern Tibet came from Australia. *Geology* **2011**, *39*, 727–730.
79. Wang, Y.; Yang, T.; Zhang, Y.; Qian, X.; Gan, C.; Wang, Y.; Wang, Y.; Senebouttalath, V. Late Paleozoic back-arc basin in the Indochina block: Constraints from the mafic rocks in the Nan and Luang Prabang tectonic zones, Southeast Asia. *J. Southeast Asian Earth Sci.* **2020**, *195*, 104333.
80. Liu, G.; Sun, Z.; Zi, J.; Santosh, M.; Zhao, T.; Feng, Q.; Chen, G.; Nie, X.; Li, J.; Zhang, S. Proto-Tethys ophiolitic mélange in SW Yunnan: Constraints from zircon U-Pb geochronology and geochemistry. *Geosci. Front.* 2021, *in press*.
81. Wood, D.A. The application of a Th-Hf-Ta diagram to problems of tectonomagmatic classification and to establishing the nature of crustal contamination of basaltsic lavas of the British tertiary volcanic province. *Earth Planet. Sci. Lett.* **1980**, *50*, 11–30.
82. Pearce, J.A.; Cann, J.R. Tectonic setting of basic volcanic rocks determined using trace element analyses. *Earth Planet. Sci. Lett.* **1973**, *19*, 290–300.

83. Harris, N.B.W.; Pearce, J.A.; Tindle, A.G. Geochemical characteristics of collision-zone magmatism. In *Geological Society*; Special Publications: London, UK, 1986; Volume 19, pp. 67–81.
84. Stern, R.J. *The Anatomy and Ontogeny of Modern Intra–Oceanic Arc Systems*; Kusky, T.M., Zhai, M.G., Xiao, W., Eds.; The Evolving Continents: Understanding Processes of Continental Growth; Geological Society: London, UK; Special Publications: London, UK, 2010; Volume 338, pp. 7–34.
85. Deering, C.D.; Vogel, T.A.; Patino, L.C.; Alvarado, G.E. Origin of distinct silicic magma types from the Guachipelín Caldera, NW Costa Rica: Evidence for magma mixing and protracted subvolcanic residence. *J. Volcanol. Geotherm. Res.* **2007**, *165*, 103–126.
86. Wilson, W. *Igneous Petrogenesis*; Unwin Hyman: London, UK, 1989; pp. 327–373.
87. Tran, V.T.; Vu, K.; Vu, (Eds.). *Geology and Earth Resources of Vietnam, General Dept of Geology, and Minerals of Vietnam, Hanoi*; Publishing House for Science and Technology: Hanoi, Vietnam, 2011; p. 634.
88. Thanh, T.-D.; Phuong, T.H.; Janvier, P.; Nguyen, H.H.; Nguyen, T.T.C.; Nguyen, T.D. Silurian and Devonian in Vietnam-stratigraphy and facies. *J. Geodyn*. **2013**, *69*, 165–185.
89. Maluski, H.; Lepvrier, C.; Leyreloup, A.; Van Tich, V.; Thi, P.T. 40Ar-39Ar geochronology of the char-nokites and granulites of the Kan Nack complex, Kon Tum Massif, Vietnam. *J. Asian Earth Sci*. **2005**, *25*, 653–677.
90. Roger, F.; Maluski, H.; Leyreloup, A.; Lepvrier, C.; Thi, P.T. U–Pb dating of high temperature metamorphic episodes in the Kon Tum Massif (Vietnam). *J. Southeast Asian Earth Sci.* **2007**, *30*, 565–572.
91. Hrichi, S.; Chaabane-Banaoues, R.; Bayar, S.; Flamini, G.; Oulad El Majdoub, Y.; Mangraviti, D.; Mondello, L.; El Mzoughi, R.; Babba, H.; Mighri, Z.; et al. Botanical and Genetic Identification Followed by Investigation of Chemical Composition and Biological Activities on the *Scabiosa atropurpurea* L. Stem from Tunisian Flora. *Molecules* **2020**, *25*, 5032.
92. Pradaa, M.; Ranerob, C.R.; Sallaresa, V.; Grevemeyerc, I.; deFrancod, R.; Gervasie, A.; Zitellinig, N. The structure of Mediterranean arcs: New insights from the Calabrian Arc subduction system. *Earth Planet. Sci. Lett.* **2020**, *548*, 116480.
93. Handy, M.R.; Schmid, S.M.; Bousquet, R.; Kissling, E.; Bernoulli, D. Reconciling plate-tectonic reconstructions of Alpine Tethys with the geological–geophysical record of spreading and subduction in the Alps. *Earth-Sci. Rev*. **2010**, *102*, 121–158.
94. Loreto, M.F.; Zitellini, N.; Ranero, C.R.; Palmiotto, C.; Prada, M. Extensional tectonics during the Tyrrhenian back-arc basin formation and a new morpho-tectonic map. *Basin Res.* **2020**, *33*, 138–158. https://doi.org/10.1111/bre.12458.